UMEÅ UNIVERSITY

MRI in prostate cancer

Implications for target volume

Ulrika Björeland

Department of Radiation Sciences, Radiation Physics
Umeå 2023

This work is protected by the Swedish Copyright Legislation (Act 1960:729)
Dissertation for PhD
ISBN: 978-91-7855-988-6 (print)
ISBN: 978-91-7855-989-3 (pdf)
ISSN: 0346-6612
New Series Number 2225
Electronic version available at: http://umu.diva-portal.org/
Printed by: Cityprint i Norr AB
Umeå, Sweden 2023

What I love about science is that as you learn, you don´t really get answers.

You just get better questions.

-John Green

Table of Contents

Abstract ..... **iii**

Abbreviations ..... **v**

Sammanfattning ..... **vi**

List of publications ..... **viii**

Thesis overview **1**

Aims of the thesis 1

Summary of papers 2

Ethical considerations 3

Introduction **4**

Cancer Biology 4

Prostate cancer biology and classification *6*

MRI, basic principles and applications 10

Basic principles of MRI *10*

Magnetic resonance imaging in Prostate Cancer *19*

CT, basic principles and applications 24

PCa imaging in CT *24*

PET/CT, basic principles and applications 24

PCa imaging in PET *26*

External radiotherapy 27

Images for treatment planning *27*

Target definitions *28*

Treatment alternatives in PCa 29

Treatment strategies for high-risk and very high-risk PCa *30*

Methods **33**

Contour propagation 34

Image processing 35

Movement analysis in the target volume 36

Target imaging 37

Target identification *37*

Hyaluronic acid-spacer, stability and rectum dosimetry 39

Pre-treatment imaging 40

Results **41**

Movement analysis in the target volume 42

Target imaging 43

Hyaluronic acid-spacer, stability and rectum dosimetry 43

Pre-treatment imaging 45

Discussion **47**

Target imaging 47

Target movements 48

Target delineation 49

Strengths and weaknesses of this doctoral project 51

Future perspectives **52**
Conclusions **53**
Acknowledgements **54**
References **55**

Abstract

Prostate cancer (PCa) is the most common cancer among men, with 10 000 new cases per year in Sweden [1]. To diagnose PCa, magnetic resonance imaging (MRI) is used to identify and classify the disease. The patient's treatment strategy depends on PCa classification and clinical data, which are weighted together into a risk group classification from 1–5. For patients with higher risk classes (>3), radiotherapy together with hormone therapy is a common treatment option [2].

In radiotherapy (RT), individual treatment plans are created based on the patient's anatomy. These plans are based on computed tomography (CT), often supplemented with MRI images. MRI and CT complement each other, as MRI has better soft tissue contrast and CT has better bone contrast. Based on the images, the volumes to be treated (target) and the volumes to be avoided (risk organs) are defined. Prostate RT is complex, and there are uncertainties regarding the patient's internal movements and how the patient is positioned before each treatment. To account for these uncertainties, the radiation field is expanded (extended margins to target) to ensure that the treatment volume receives its radiotherapy. RT is most often given in fractions. Fractionation, dose, and treatment volume depend on the patient's risk category. The treatment area can be, for example, only prostate, prostate with extra radiation dose (boost) to an intraprostatic tumour, or prostate with lymph node (LN) irradiation. LN irradiation is most often given for preventive purposes for PCa with a risk classification >4, which means no cancer has been identified, but any microscopic spread to the LNs is being treated profylactically.

In RT, target identification is essential both in the treatment planning images (CT/MRI) and at treatment. Studies have shown that PCa often re-occurs in or near the volume of the dominant (often largest) intraprostatic tumour [3, 4], and this volume is relevant for boosting. For patients treated with hormone therapy before radiotherapy, tumour identification is complicated. Hormones change the tumour characteristics, affecting the image contrast and making the tumour difficult to identify. To study this, we investigated whether texture analysis could identify the tumour volume after hormone therapy (paper II). However, even with texture analysis, the tumour was difficult to identify. A follow-up study examined whether the image information in MRI images taken before hormone therapy could indicate how the treatment fell out (paper IV). However, no correlation was seen between image features and the progression of PCa.

Identifying the target and correctly positioning the patient for each treatment fraction is the most important procedure in radiotherapy. The prostate is a mobile organ; therefore, intraprostatic fiducial markers are inserted before treatment planning to reduce positioning uncertainties. Each radiotherapy session begins with an X-ray image where the markers are visible, and the radiation can be

delivered based on the markers' position. The markers are also used as guidance for large target volumes, such as for prostate with LN irradiation. With better knowledge of the prostate and LN movements, the margins can potentially be reduced, followed by reduced radiation dose to healthy tissue and therefore reduced side effects for patients. Movements in the radiotherapy volume were the focus of paper I. Using MRI images, the movements of the prostate and LNs were measured during the course of radiotherapy, and we found that LN movement is independent of the movement of the prostate and that the movement varies in the target volume.

In addition to the recurrence of PCa in the tumour area, there is an increased risk of recurrence in the prostate periphery close to the rectum. Since the rectum and prostate are in contact for some patients, RT must be adapted to make rectum side effects tolerable. One way to increase the distance between the prostate and the rectum is to inject a gel between the two organs. The distance makes it easier to achieve a better dose distribution to the PCa. This idea resulted in paper III, where patients were given a gel between the prostate and rectum. MRI was used to check the stability of the gel during the course of RT and was evaluated together with long-term follow-up of the patient's well-being and acceptance of the gel. We found that the radiation dose to the rectum was lower with a spacer, although the spacer was not completely stable during treatment.

In this thesis, I look at four tasks where we have tried to improve radiation therapy for the patient with the help of MRI. Improving the identification of the target volume leads to safer RT and increased quality of life for the patient.

Abbreviations

ACE	11C Acetate
ADC	Apparent diffusion coefficient
ADT	Androgen Deprivation Therapy
A-P	Anterior-posterior direction
b	Diffusion sensitisation factor
Bo	External magnetic field
B1	Added magnetic field
C-C	Cranio Caudal direction
COM	Centre Of Mass
CRS	The space between CTV and rectum
CSF	Cerebrospinal fluid
CT	Computed Tomography
CTV	Clinical Target Volume
DCE	Dynamic Contrast-Enhanced
DIL	Dominant Intraprostatic Lesion
DIR	Deformable (or nonrigid) Image Registration
DNA	Deoxyribonucleic acid
DVF	Deformation Vector Field
DWI	Diffusion-Weighted MRI
EM	Electro Magnetic
EPI	Echo Planar Imaging
FDG	18F fluorodeoxyglucose
FID	Free Induction Decay
FTV	Functional Tumour Volume
G	Gradient
Gd	Gadolinium
GLCM	Grey-Level Co-occurrence
GRE	Gradient echo
GTV	Gross Tumour Volume
HA	Hyaluronic Acid
HR	High-Risk (PCa)
HU	Hounsfield Units
Ktrans	Kinetic parameter calculated from DCE imaging
Linac	Linear accelerator
LN	Lymph Node
M	Magnetisation vector
MI	Mutual Information
mpMRI	Multiparametric MRI
MRI	Magnetic resonance imaging
NUS	Norrlands Universitetssjukhus (Umeå University Hospital)
OAR	Organs At Risk
PCa	Prostate Cancer
PET	Positron Emission Tomography
PI-RADS	Prostate Imaging -Reporting and Data System
PSA	Prostate-Specific Antigen
PSMA	Prostate-Specific Membrane Antigen
PTV	Planning Target Volume
RF	Radio Frequency
R-L	Right-Left direction
ROI	Region Of Interest
RR	Rigid Image Registration
RT	Radiation Therapy or Radiotherapy
sCT	Synthetic CT
SE	Spin Echo
SUV	Standardised Uptake Value
T	Tesla
T1w	T1 Weighed MRI
T2w	T2 Weighed MRI
TE	Echo Time
TLA	Total Lipogenic Activity
TNM	Classification of Malignant Tumours
TP	Treatment Planning
TPS	Treatment Planning System
TR	Repetition Time
VHR	Very High-Risk (PCa)
VMAT	Volumetric Arc Therapy
VOI	Volume of Interest
WPRT	Whole Pelvis Radiotherapy including lymph node chain
γ	Gyromagnetic ratio
ωo	Larmour frequency

Sammanfattning

Prostatacancer (PCa) är den vanligaste cancerformen bland män med 10000 nya fall per år i Sverige [1]. För att diagnosticera PCa görs bland annat en magnetkameraundersökning (MRT) där den sjukdomen identifieras och klassificeras. Patientens behandlingsstrategi beror på PCa klassificering och kliniska data, som vägs ihop till en riskgruppsklassificering från 1-5. För patienter med högre riskklasser (>3) är strålbehandling tillsammans med hormonbehandling ett vanligt förekommande behandlingsalternativ [2].

Vid strålbehandling skapas individuella dosplaner utifrån patientens anatomi. Dessa bygger på datortomografibilder (DT), insamlade i patientens planerade behandlingsposition, ofta kompletterade med MRT bilder. MRT och DT kompletterar varandra då MRT har bättre mjukdelskontrast medan DT har bättre benkontrast. Baserat på bildunderlaget definieras de volymer som ska behandlas (target) samt de volymer som skall undvikas (riskorgan). Strålbehandling av prostata är komplext och det finns osäkerheter gällande både patients inre rörelser och hur patienten positioneras inför varje behandling. För att ta hänsyn till dessa osäkerheter utökas strålfältet (utökade marginaler till target) för att säkerställa att behandlingsområdet får sin strålbehandling. Strålbehandling ges oftast i fraktioner. Fraktionering, dos samt behandlingsområde beror på vilken riskkategori patienten tillhör. Behandlingsområdet kan tex vara: endast prostata, prostata med extra stråldos (boost) till en intraprostatisk tumör eller prostata med lymfkörtelbestrålning. Lymfkörtelbestrålning ges oftast i förebyggande syfte för avancerad PCa (över klass 4). Ingen cancer har identifierats, men eventuell mikroskopisk spridning till lymfkörtlarna behandlas preventivt.

Grunden för all strålbehandling är att kunna identifiera target både i dosplaneringsbilderna (DT/MRT) och vid behandlingstillfället. Studier har visat att det är i området där den dominanta (ofta största) intraprostatiska tumören funnits som risken är störst för canceråterväxt [3, 4]. Det är dessa områden som är aktuella för boosting. För patienter som behandlas med hormonbehandling i samband med strålbehandlingen kompliceras detta ytterligare då tumörens egenskaper förändras, vilket även påverkar bildkontrasten och tumören blir mycket svår att identifiera. För att studera detta, undersöktes om man med texturanalys kunde identifiera tumörområdet efter hormonbehandling (papper II) men även med texturanalys visade det sig att tumören var svår att identifiera. I en uppföljande studie undersöktes om bildinformationen i MRT-bilder tagna före hormonbehandlingen kan spegla behandlingsresultatet (papper IV).

Identifiering av target och att kunna positionera patienten korrekt inför varje behandlingsfraktion är det viktigaste då strålbehandlingen ska ges. För att

reducera osäkerheter i positioneringen av patienten, sätts markörer in i prostata inför behandlingen. Prostatan är ett rörligt organ och varje strålbehandlingstillfälle inleds med en röntgenbild där markörerna syns och strålbehandlingen kan sedan riktas in utifrån denna position. Vid behandlingar av ”prostata med lymfkörtelbestrålning” används också markörerna som riktmärken för hela strålbehandlingsvolymen. Med bättre kunskap om rörelserna kan marginalerna potentiellt krympas vilket skulle minska stråldosen till frisk vävnad och därmed minska biverkningarna för patienterna. Lymfkörtlarnas rörelse i strålbehandlingsområdet var fokus för papper I. Med hjälp av MRT bilder uppmättes prostatans och lymfkörtlarnas rörelser under strålbehandlingens gång och vi fann att lymfkörtlelrörelsen är oberoende av prostatans rörelse och att rörelsen varierar i strålplaneringsområdet.

Förutom återfall av PCa i tumörområdet finns ökad risk för återfall även i prostatans ytterkant som gränsar mot rektum. Eftersom rektum och prostata ligger i kontakt för vissa patienter, så måste strålbehandlingen anpassas så att inte biverkningarna från rektum blir för stora. Ett sätt att öka avståndet mellan prostata och rektum är att injicera en gel mellan prostata och rektum för att skaffa det extra utrymme som behövs för att kunna behandla PCa på önskat sätt. Denna idé utmynnade i papper III där patienter fick en gel mellan prostata och rektum. MRT användes för att kontrollera gelens stabilitet under strålbehandlingen samt som underlag för dosuppskattning till rectum. Vi fann att stråldosen till rektum blev lägre med gel, även om inte gelen var helt formstabil under behandlingens gång.

I denna avhandling har vi tittat på fyra olika moment där vi med hjälp av MRT försökt förbättra strålbehandlingen för patienten. Förbättring av strålområdets identifiering leder till säkrare strålbehandling och ökad livskvalité för patienten.

List of publications

This thesis is based on the following papers, which are referred to by their roman numerals in the text:

I. **Björeland U,** Jonsson J, Alm M. Beckman L, Nyholm T, Thellenberg-Karlsson C. " Interfraction movements of the prostate and pelvic lymph nodes during IGRT." *Journal of Radiation Oncology. 2018:4 (357-366)*

II. **Björeland U**, Nyholm T, Jonsson J, Skorpil M, Blomqvist L, Strandberg S, Riklund K, Beckman L, Thellenberg-Karlsson C. *"Impact of neoadjuvant androgen deprivation therapy on magnetic resonance imaging features in prostate cancer before radiotherapy."* Phys Imaging Radiat Oncol 2021:17 (117-123)

III. **Björeland U***, Notstam K*, Fransson P, Söderkvist K, Beckman L, Jonsson J, Nyholm T, Thellenberg-Karlsson C. *"Hyaluronic acid spacer in prostate cancer radiotherapy: dosimetric effects, spacer stability and long-term toxicity and PRO in a phase II study."* Radiation Oncology 2023 Jan 2;18 (1):1

IV. **Björeland U**, Strandberg S, Söderkvist K, Nyholm T, Jonsson J, Skorpil M, Blomqvist L, Riklund K, Beckman L, Thellenberg-Karlsson C *"Diffusion-weighted MRI and ^{11}C-acetate-PET/CT imaging in High-Risk/Very High-Risk Prostate Cancer"* Manuscript

* shared first authorship

Thesis overview

This thesis begins with the aims and a short table overview of the included papers, followed by ethical considerations. After that, sections describe general PCa biology, magnetic resonance physics and sequences. Also, a brief introduction to computed tomography and positron emission tomography will be presented. Only external beam radiation will be covered in the radiotherapy section, focusing on high-risk or very high-risk PCa.

Aims of the thesis

This thesis aims to solve problems we noticed when implementing magnetic resonance imaging (MRI) in prostate cancer (PCa) radiotherapy (RT) and the clinical studies followed by MRI in RT. We used MRI to evaluate movements, tumour contrast after hormone therapy, dose sparing with spacers, and imaging in correlation to the outcome, all conditions that influence target volumes in different ways. This evaluation was performed to improve PCa RT.

Specific aims

I. To evaluate interfraction movements of lymph node regions that are commonly included in the pelvic clinical target volume (CTV) for high-risk prostate cancer patients. We also aimed to evaluate whether the movements affect the planning target volumes.

II. To identify intraprostatic tumour lesions after neoadjuvant androgen deprivation therapy using texture analysis.

III. To evaluate the impact of an HA perirectal spacer on rectal dose as well as spacer stability during RT with a five-year follow-up of patient-reported outcome (PRO) and gastrointestinal (GI)/genitourinary (GU) toxicity in conventionally fractionated definitive RT in prostate cancer.

IV. To evaluate if pretreatment image features in prostate gross tumour volume (GTV) correlate to treatment response and oncological parameters in high-risk/very high-risk prostate cancer.

Summary of papers

Table 1 presents an overview of the included papers and will be described in more detail in the Methods and Results sections.

Table 1. Overview of the included papers in the thesis.

	Dataset	Approach	Data analysis	Main findings
Paper I	10 patients from MOVE study. MRI on six occasions during the RT process.	Movement measurements of LNs and prostate during RT.	Deformable image registration with anatomical landmarks as reference.	LNs move independently of the prostate movements.
Paper II	50 patients from PARAPLY study. MRI before and after ADT.	Can texture feature analysis improve tumour detectability after ADT?	Deformable image registration and volume transfer from baseline to images after ADT. Feature evaluation in the volumes.	The median ADC value could differentiate significantly between tumour and reference tissue after ADT, but the texture features did not.
Paper III	52 patients from NOHARM study. MRI before and three sessions after HA.	HA spacer: its stability and influence on rectum dosimetry	HA stability evaluation with deformable image registration and dosimetric impact during RT.	HA spacer reduced the rectal dose. HA was stable after approximately 30 days and throughout the treatment.
Paper IV	76 patients from PARAPLY study. Acetate-PET/CT and MRI ADC imaging before ADT and RT.	ADC and Acetate uptake in GTV and correlation to oncological parameters and outcome.	Descriptive statistics.	Imaging features correlate weak/moderately to oncological parameters but not to outcome.

Ethical considerations

All procedures in papers I–IV followed the Regional Ethics Board and the 1964 Declaration of Helsinki and its later amendments or comparable ethical standards [5]. Patients in the different studies were recruited consecutively during their consultation at Norrlands universitetssjukhus after being given both oral and written patient information and time to consider the offer to participate. All studies included in the thesis have received ethical approval from the Regional Ethical Review Board in Umeå.

Study I was approved in 2013 (Dnr 2013-3-31 M). Study II+IV was also approved in 2013 (Dnr 2013-154-31) and Study III in 2009 (DNR 09-227 M/2009-1433-31) with a complement in 2011 (Dnr 2011-188-32 M).

All studies were planned more than ten years ago. The technical improvements in both radiotherapy and diagnostic imaging have been considerable since then. Radiotherapy has been improved by more advanced techniques for dose delivery and better imaging possibilities on the linear accelerator (linac). When diagnosing PCa, the MRI images are of better quality, and an international guide for PCa identification is implemented for standardisation. In positron emission tomography (PET) imaging, Prostate-Specific Membrane Antigen (PSMA) has shown promising results as a PCa tracer, and acetate, which was used in paper IV, is rarely used. Therefore, it is of great importance, both ethically and scientifically, that we publish results even though some techniques might be outdated and replaced because the knowledge we gathered is one piece of the puzzle for better RT in PCa. Publishing results, both positive and negative, is the researchers' responsibility to the patients who voluntarily participated in studies and contributed to greater knowledge about PCa treatments.

Introduction

Magnetic resonance imaging uses magnetic fields to visualise tissue properties [6]. MRI has an excellent soft tissue contrast and is essential in prostate cancer imaging [7]. This introduction begins with an overview of prostate cancer and its biology, followed by MRI theory and sequences for PCa applications. Also, other imaging modalities in PCa will be described briefly. See Figure 1 for representative imaging. The last sections cover external beam RT for PCa according to the Swedish guidelines [2] and how MRI can be useful for RT target identification.

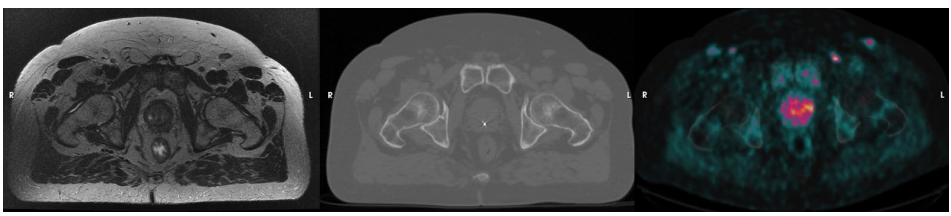

Figure 1. PCa images from PARAPLY study. Left: T2w MRI with a superior soft tissue contrast compared to CT (middle) and acetate PET/CT (right). Acetate uptake is related to lipogenic activity, which is increased in PCa.

Cancer Biology

Human body tissues consist of cells, and in the cell core, there is deoxyribonucleic acid (DNA)[8, 9]. DNA is built from organic molecules (nucleotides) and contains information about the function and development of the cells. DNA can be compared to a recipe or a code with information about cell function [9]. The part of the DNA that regulates these functions is the genes. The gene consists of a specific sequence of nucleotides at a given position on a given DNA formation (chromosome) that codes for a specific protein [8, 9].

The DNA consists of two strands [8, 9]. Each strand consists of polynucleotides composed of nucleotides. The nucleotide sequence combination is the genetic code that regulates all functions in the body [8].

In cell multiplication, chromosomes are replicated into two identical parts before cell division (mitosis) [8, 9]. Cells are continuously replaced, and the number of cells is controlled by signals regulating cell death and the creation of new cells. In general, cancers [10] are cells that multiply uncontrollably, caused by damaged DNA, and a cancerous tumour may be formed. DNA damage (mutations) can be of random nature (mishappening in replication) or induced by chemicals or several physical agents, such as UV light and gamma radiation [11]. Cancer can

develop if the mutation occurs in a gene controlling cell growth. The cancerous tumour can grow rapidly and prevent the body from functioning properly [8, 9].

Almost all types of cancers follow the same cycle: first, the cells start to replicate (proliferate) uncontrollably and can sustain chronic proliferation [9]. The signals that regulate start/stop in cell proliferation are overruled. These new cells need oxygen and nutrients to proliferate, and new vessels are produced [12, 13]. These new vessels are created from the normal tissue vasculature but are of an irregular pattern, more brittle, and admit slower blood flow than the vasculature in normal tissue [13]. Rapid cell division demands more nutrients, and cancer cells consume more glucose than normal tissue [9]. All these factors contribute to cancer development following tissue invasion and metastasis. How a disease metastasises and how metastatic cells alter from their origin cell and adapt to a new environment are under research [14]. What is known is that metastasis is a major cause of death for cancer patients [14].

Radiation can cause DNA damage, which is used in RT to treat cancer [8, 15]. When radiation travels through tissue, energy is deposited along its ionising track. This energy depletion causes changes in the chemical environment and induces lesions in the DNA [8]. Further, radiation can also, via direct action to the DNA, damage the strands [8]. DNA can undergo single- or double-strand breaks from ionising radiation, which can lead to a biological effect (mutation). A single-strand break is more likely to be repaired correctly than a double-strand break [8]. Radiation-induced cell damage are classified as either acute or late effects, according to the time before the appearance of symptoms. Acute (early) effects are observed within a few weeks after treatment, and late effects emerge months to years after radiation exposure [16].

The ability to repair radio-induced strand breaks (the radiosensitivity) differs between organs [16]. Acute radiation damage affects tissues with rapidly proliferating cells, such as in epithelial surfaces of the skin or alimentary tract. Late effects occur in tissues with slow cell renewal, such as subcutaneous tissue, fatty tissue, muscle, brain, kidney, and liver and in slow proliferation sites within tissues containing rapidly-proliferating cells, such as the wall of the intestine. There are many possible side effects of RT PCa [17]. Acute side effects include diarrhoea from loss of integrity of the epithelium and increased secretion of mucus. The late effects are increased stool frequency, urgency, spotting of blood, and partial incontinence [16].

Prostate cancer biology and classification

The prostate gland is an organ composed of various types of tissue [18]. It consists of fibrous, elastic, connective, glandular, nerve, vascular, lymphatic, and a small amount of striped muscular tissue. The prostate is a male reproductive androgen-regulated organ. Androgens are a prerequisite for the normal prostate, and the prostate has various functions, including producing seminal fluid. It produces approximately one-third of the total seminal fluid (a component in semen); the seminal vesicles produce the rest. Another vital element of semen is the prostatic-specific antigen (PSA) protein.

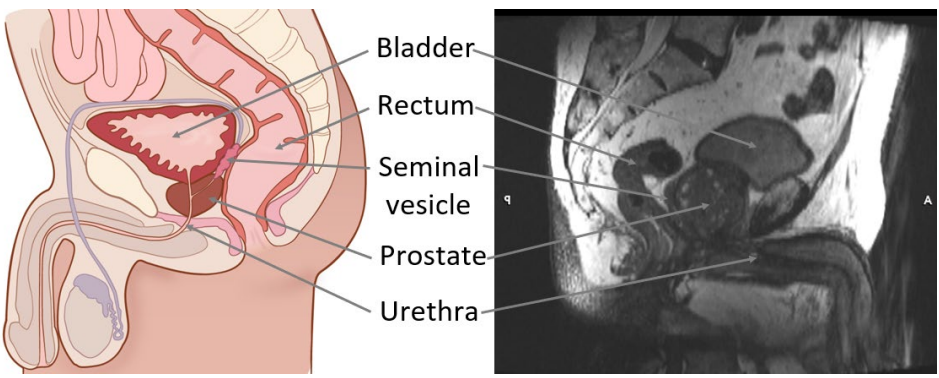

Figure 2. Schematic anatomy overview (left), T2w MRI from MOVE study (right). The bladder, rectum and urethra are organs near the prostate and must be considered in radiotherapy with dose constraints. Case courtesy of Johan Röstwall (schematic anatomical overview).

The normal prostate is shaped like a walnut, weighs 15–20 g, and is 3-cm long. The prostate gland is located in the male pelvis (Figure 2). It is below (inferior) the urinary bladder and immediately anterior to the rectum. The prostate gland encircles the posterior part of the urethra [18-21].

The prostate gland is divided into zones of distinct histopathologic appearance: the transition zone, central zone, periurethral zone, and peripheral zone [21]. Central is a cone-shaped region, with the wider portion at the base of the prostate and comprises 25% of normal prostate volume. The transitional zone is located centrally and surrounds the urethra, comprising approximately 5% of normal prostate volume. The peripheral zone is the main part of the gland (approximately 70%) and is located posteriorly in the prostate [18, 21]. See Figure 3.

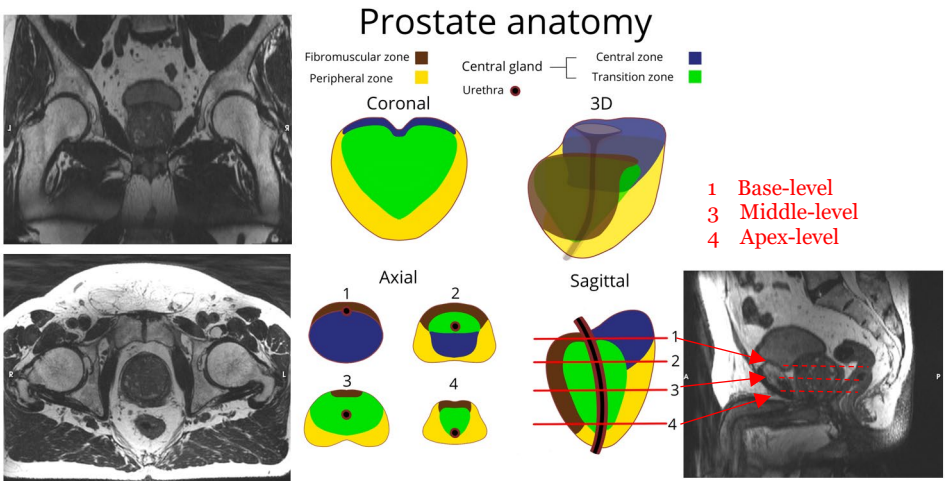

Figure 3. Overview of Prostate anatomy and zones. MRI T2w images from MOVE study, top left Coronal orientation, bottom left Axial/Transversal orientation, bottom right Sagittal orientation. Schematic overview of the prostatic anatomy with case courtesy of David Gendy, Radiopaedia.org, rID: 93412.

The most common PCa sites are in the peripheral zone (70%) and the transition zone (25%). In normal prostate tissue, glandular cells are stimulated by androgens for growth. PCa begins with a mutation in normal prostate glandular cells, and an androgen-consuming nodule is formed. Most PCa types are adenocarcinoma (95%) and spread from the mutation site to the immediately surrounding prostate tissue, forming a tumour nodule. Castrate-resistant tumours are thought to generate intracellular androgens and will not respond to the loss of androgen when the tumour is self-sufficient [18, 20, 22].

PSA is produced in normal prostatic tissue and is found in high levels in the seminal fluid [2, 23, 24]. Small amounts of PSA normally leak into the blood and can be measured. PSA increases with age due to enlarged prostate volume (number of cells) by age. PSA may also increase due to inflammation of the prostate gland (prostatitis) or PCa. PCa cells often produce less PSA than normal cells, and the raised PSA in PCa is due to increased leakage of PSA from tumour tissue into the bloodstream. This leakage is almost tenfold in PCa compared to benign prostate enlargement [2]. A PSA test can help distinguish PCa from benign prostate enlargement. The normal PSA level varies with age, and the recommendation for further investigation is PSA levels over 3 ng/ml for men

under 70 years, PSA ≥ 5 ng/ml for men 70–80 years, and PSA ≥ 7 ng/ml for men over 80 years old [2].

A high PSA can indicate PCa but also a the potential spread outside prostate. PCa spread to the bones is rare as long as the PSA value is below 10 ng/ml , whereas most PSA values above 100 ng/ml indicates a spread to lymph nodes (LNs) or bones [25]. Localised, high-risk cancer often has micrometastases, so even if a metastasis investigation with medical imaging does not show any spread, treatment principles for advanced disease can be applied [2].

TNM classification

The Classification of Malignant Tumours (TNM) is used to classify the extent of the spread of cancer. The T category describes the primary tumour site, the N category describes the regional LN involvement, and the M category describes the presence of metastatic spread [26].

For PCa, the classification for tumour extent, T, is graded from 0 to 4 [2]. T0 corresponds to no tumour that could be found up to T4 when the tumour grows into other structures, such as vesicles, pelvic wall, and rectum. T1 and T2 are localised tumours with boundaries inside the prostate gland. T3, groups tumours that have grown outside the prostate capsule: T3a describes tumours that invade the connective tissue and T3b describes tumours that invade one or both seminal vesicles. Tx indicates that the main tumour cannot be measured.

PCa spreads to the pelvic LNs along the common, internal, and external iliac [27, 28]. LN involvement is classified from N0 (no regional LN) to N1 (regional LN metastasis). LNx is used if cancer in nearby LNs cannot be measured [2]. When cancer has spread outside the regional LNs, the classification is M1a. When metastases are found in the skeleton, the classification is M1b. M0 indicates that no metastases could be proven, and Mx indicates that metastasis cannot be measured [2]. Node engagement can be detected using MRI, computed tomography (CT) or PET/CT, and bone scintigraphy can also detect metastases in bones [2].

Table 2. Gleason sum score and ISUP grade [29].

ISUP grade score	Gleason sum
1	⩽ 6
2	3 + 4
3	4 + 3
4	8
5	9 – 10

PCa characteristics are based on TNM and the pathological characteristics from biopsies. Gleason score is based on cellular patterns in structured biopsy samples and scored from 1 to 5. Gleason classification is based on the score for the most common dominating pattern added together with the highest of the other scores found in the sample [2]. The Gleason sum score is divided into five groups according to the International Society of Urological Pathology (ISUP) [29] (Table 2). All information about the PCa is combined into risk group classifications from 1 to 5 (Table 3). Risk group classification is used to determine treatment options.

Table 3. PCa risk classification according to Swedish guidelines [2].

PCa Risk		
1	Very low risk	T1c*, Gleason sum 6, ≤ 8 mm cancer in total 1–4 of 8–12 systematic biopsies, PSA < 10 ng/ml and PSA-density < 0.15 ng/ml/cm^3
2	Low risk	T1–T2a*, Gleason sum 6 and PSA < 10 ng/ml
3	Intermediate risk (favourable or unfavourable)	T2b-T2c* and/or Gleason sum 7 and/or PSA 10–19 ng/ml
4	High risk	T3 or Gleason sum 8 or Gleason sum 4+3=7 in more than 50% of the biopsies or Gleason sum 4+3=7 in guided biopsies in PI-RADS 5 lesions or PSA 20–49 ng/ml
5	Very high risk	Two or more HR factors or T4* and/or Gleason sum 9–10 and/or PSA ≥ 50 ng/ml or N1.

* T-stadium based on palpation

MRI, basic principles and applications

Magnetic resonance imaging which has excellent soft tissue contrast, uses magnetic fields to visualise tissue properties such as proton density and T1/T2 relaxation [30]. In addition to the visualization of tissue contrasts, MRI can detect and quantify water diffusion and blood flow [30].

In short, MRI is possible due to the atom nucleus's inherent nuclear spin and the presence of a strong magnetic field. This phenomenon can be explained by quantum mechanics, classical mechanics, or a mixture of both [6, 31, 32]. Based on these references, a more detailed explanation is described in the following sections.

Basic principles of MRI

The nucleus consists of protons and neutrons, and their combined configuration gives rise to a spin of the nucleus. The human body consists mainly of hydrogen-based materials such as water and lipids. The hydrogen atom has a nucleus consisting of a positively charged proton with an orbiting electron. Hydrogen nuclei have a 1/2 spin configuration due to an odd number of protons and neutrons. This half-spin state gives rise to energy levels that spin up or spin down and are the foundation of the MRI technique. In routine clinical practice, we often refer to MRI as proton imaging for simplicity.

The proton is constantly spinning and therefore creates its own local magnetic field. The proton magnetic moment is randomly oriented when outside a strong magnetic field. However, in a strong external magnetic field (B0), the protons start to rotate/wobble (precession) and will either align with (spin up) or oppose (spin down) the B0 field depending on the energy state.

The alignment with the magnetic field requires the least energy and is therefore preferred. This results in a net magnetisation vector (M) of all the protons (Figure 4).

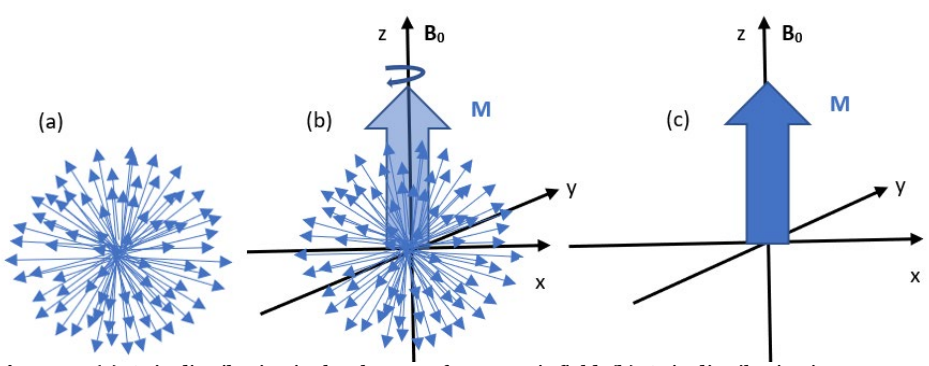

Figure 4. (a). Spin distribution in the absence of a magnetic field. (b). Spin distribution in an external magnetic field B0 (c). Net magnetisation vector M, the vector sum of all spin distributions.

In a clinical MRI, B0 is between 0.5–3 Tesla (T). For example, if B0 is 1.5 T and the temperature is 37° C, approximately 1 x 10^6 protons are aligned opposite to the magnetic field and 1.000004 x 10^6 protons are aligned with the magnetic field. A 70 kg person contains approximately 45 x 10^{27} protons. This large amount of protons in the body is the key to proton imaging.

Further, when a proton is placed in a strong magnetic field, it starts to precess with the Larmour frequency (ω0) depending on B0 and the gyromagnetic ratio (γ) as

$$\omega_0 = B_0\gamma \leftrightarrow v_0 = \frac{\gamma}{2\pi}B_0\,, [\mathrm{Hz}] \qquad (1)$$

v_o = precession frequency, sometimes referred to as Larmour frequency
γ = gyromagnetic ratio
B_o= main magnetic field

This frequency is also the frequency of the electromagnetic (EM) field that can induce a transition between two energy states. When this transition is induced (and electromagnetic energy is absorbed), the EM field is said to be in resonance with the transition frequency.

Measuring the signal, excitation and relaxation
To create an image, the net magnetization must be measured. However, the net magnetization cannot be measured when in equilibrium (M0). M0 is not time-varying and thus not detected by Faraday induction. Faraday's law states that a changing magnetic field induces a (measurable) voltage in a circuit (coil). However, if a second magnetic field, B1, is applied, the net magnetisation is tipped into the transverse (xy) plane, and the equilibrium is disrupted (Figure 5).

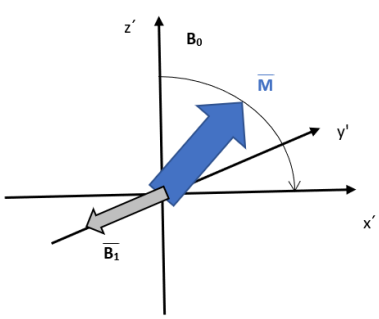

Figure 5. Rotating frame display. Magnetisation vector M precesses around B1 when B1 is on resonance. The angle between M and x' is called the flip angle.

All the spins are collectively rotated away from the z-axis with a flip angle. This magnetic field, B1, is known as the radio frequency (RF) pulse or excitation pulse. B1 is much weaker than B0, as is measured in μ T rather than T. When M is tipped into the xy-plane, the Mxy component can be measured by Faraday induction of an electric force in an RF receiver coil. Usually, a pair of receiver coils are used. These are connected to sensitive amplifiers that are tuned to the Larmor frequency, and only the component of the magnetization in the xy-plane is detected. This signal is called free induction decay (FID) [32] (Figure 6).

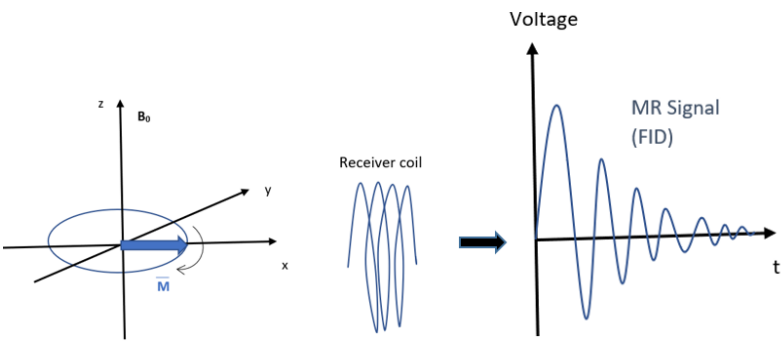

Figure 6. Simplified illustration of signal detection in MRI using a receiver coil in which an alternating voltage of resonance frequency is induced.

The detected signal in the receiver coil is a time- and amplitude-varying voltage at the resonance frequency and lasts for tens of milliseconds. When the RF is turned off, the system returns to equilibrium. How fast this process takes depends on inherent tissue properties and is referred to as the relaxation process. There are two types of relaxation: longitudinal and transversal relaxation. The relaxation occurs as soon as the RF is turned off.

Longitudinal relaxation (T1 relaxation or spin-lattice relaxation) is obtained when the RF is turned off and the protons relax back to equilibrium (Figure 7). The time it takes to return to equilibrium depends on how fast the obtained energy from RF is released to the surrounding tissue (lattice). As soon as the RF is turned off, the Mz will start to grow. The extent of the growth of the Mz depends on the T1 characteristics for the tissue, as expressed in equation 2:

$$Mz = M_0\left(1 - e^{-t/T1}\right) \qquad (2)$$

T1 is the time constant referring to longitudinal relaxation (Figure 7).

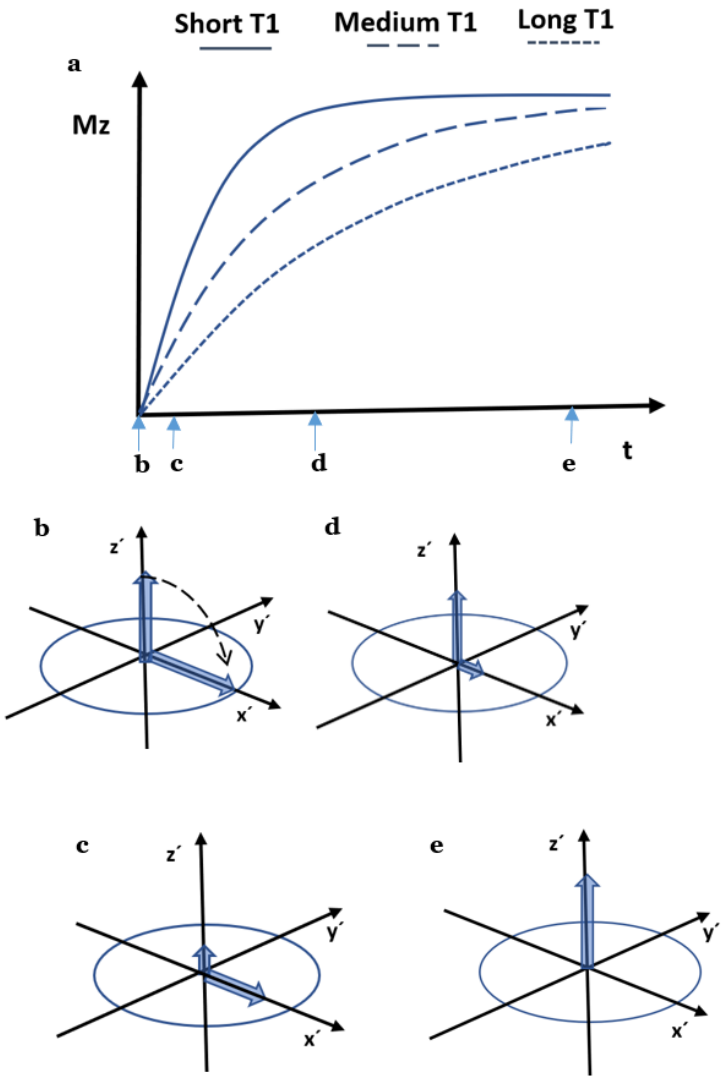

Figure 7. Illustration of the relaxation process. a. Regrowth of Mz due to T1 (longitudinal) relaxation for different tissues with different T1 times. b. Magnetisation vector tipped into the transversal plane. c and d. Recovery of the signal. e. Magnetisation fully recovered.

Transversal relaxation (T2 relaxation or spin–spin relaxation) starts when the RF is turned off and the phase coherence starts in the xy-plane (Figure 8). T2 is the time constant for the decay of transverse magnetization arising from interactions between atoms or molecules. These interactions create random variations in the resonance frequency and cause coherence among the proton spins. The Mxy will decrease due to the coherence directly after the RF pulses are turned off (Figure 8 and equation 3).

$$M_{xy} = M_0 e^{-t/T2} \qquad (3)$$

However, transverse magnetisation decays much faster if field inhomogeneities are present; in MRI, field variations are always present. This observed T2 (T2*) includes interactions between atoms or molecules and field inhomogeneities. The measured FID is a T2* decay.

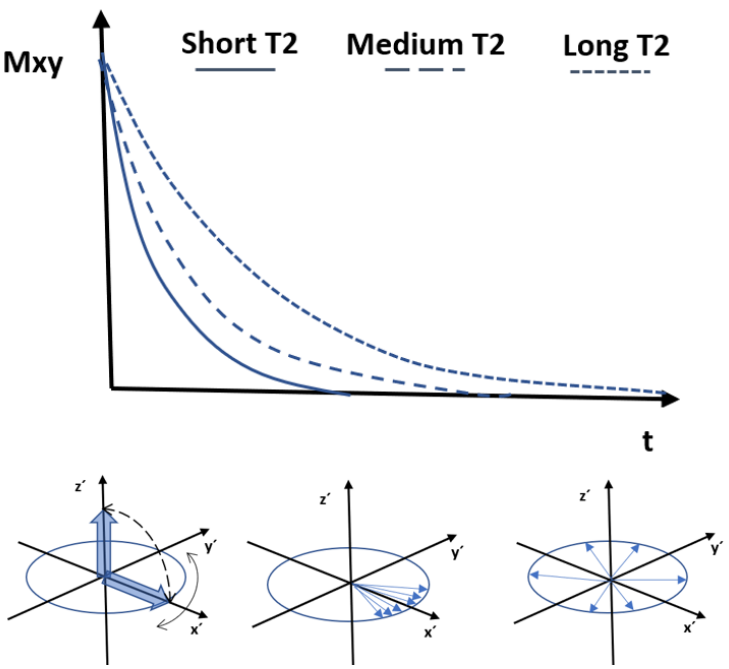

Figure 8. Illustration of the relaxation process. Regrowth of Mxy due to T2 (transversal) relaxation for different tissues with different T2 times (top). Bottom spin de-phasing.

The T1 and T2 times are tissue-specific, depend on molecule size and tumbling rate and vary with B0 [6, 33], resulting in different contrasts (Table 4). The image contrasts are created by a pulse sequence that is a structured scheme by turning the RF pulse off and on along with spatial information encoding [6, 31-33].

Table 4. Approximate T1 and T2 values at 1.5 and 3T. All values were measured in vivo from human tissues [6, 33] and for PCa T1 [34] and PCa T2 [35].

	T1 (ms)		T2 (ms)	
	1.5T	**3.0T**	**1.5T**	**3.0T**
Fat	200	382	70	68
White Matter	560	832	82	110
Liver	570	809	40	34
Muscle	1075	898	33	29
Gray Matter	1100	1331	92	80
CSF	2060	3700	2000	-
PCa	-	1301	-	105

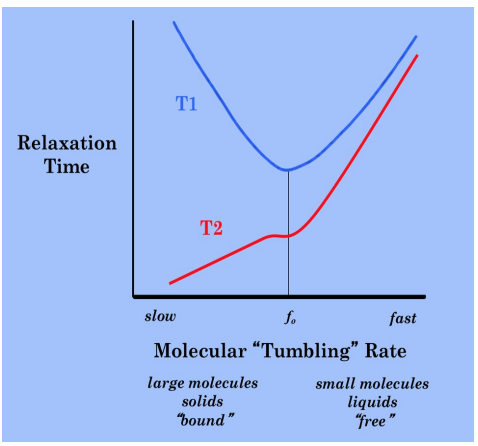

Figure 9. T 1 and T2 as a function of molecular size and tumbling rate. The minimum value of T1 and plateau on the T2 curve (accentuated for didactic purposes) occurs when motion is near the Larmor frequency. Reproduced with Courtesy of Allen D. Elster, MRIquestions.com

Spatial encoding

Now we can measure the signal, but where the information comes from is missing. To create a three-dimensional xyz-coordinate system, three additional magnetic fields (gradients) are used. The gradients are designed to vary along its axes from a low to a high magnetic field and are in the range of 30–50 mT/m. The result is that the protons will spin with different frequencies along the gradient, making localisation possible.

If the patient table is in the z-direction, x is left-right and y is the anterior-posterior direction. The first gradient applied is the z-direction (Gz), which determines where the patient images will be produced. To measure one slice, an RF pulse with a frequency that matches the proton spin in that location is applied. All protons in the slice are in phase. The slice thickness depends on the RF bandwidth. RF contains several frequencies (bandwidth) and excites protons in that range. Gz is often referred to as the slice-selecting gradient (Figure 10).

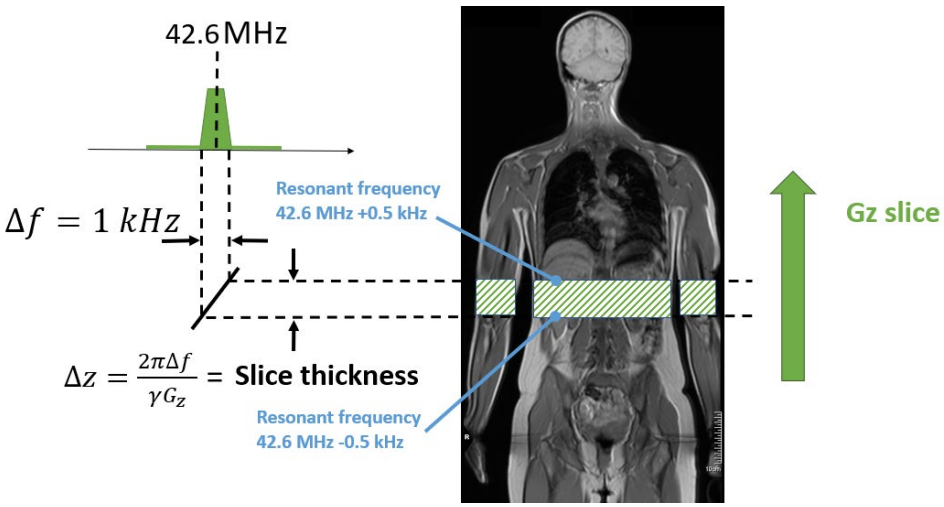

Figure 10. Slice selection in 1T magnet. Slice thickness, Δz, depends on the width of the frequency range, Δf, and the Gz-gradient applied in the z-direction and the gyromagnetic ratio γ.

Inside this slice, we apply the second gradient (Gy). Gy is applied subsequently to Gz and creates a phase variation in the y direction. When Gy is turned off, the protons relax to the equilibrium state with precession ω0 but now with different phases (Figure 11). The phase difference is due to Gy. Gy is often referred to as the phase encoding gradient. The number of phase encoding steps determines the image resolution. To achieve an image with 256 rows, 256 phase-encoding steps are needed.

The last step for localisation of the signal applies a gradient in the x-direction (Gx), which results in the spins to the left side precession being faster than the spins to the right of the patient (Figure 12). Gx is applied subsequent to Gy during the measurement of the signal (read-out). The read-out is a varying frequency received signal in the x-direction. Gx is often referred to as the frequency encoding gradient [6, 31, 32]. In (Figure 11) the phase and frequency encoding is visualised.

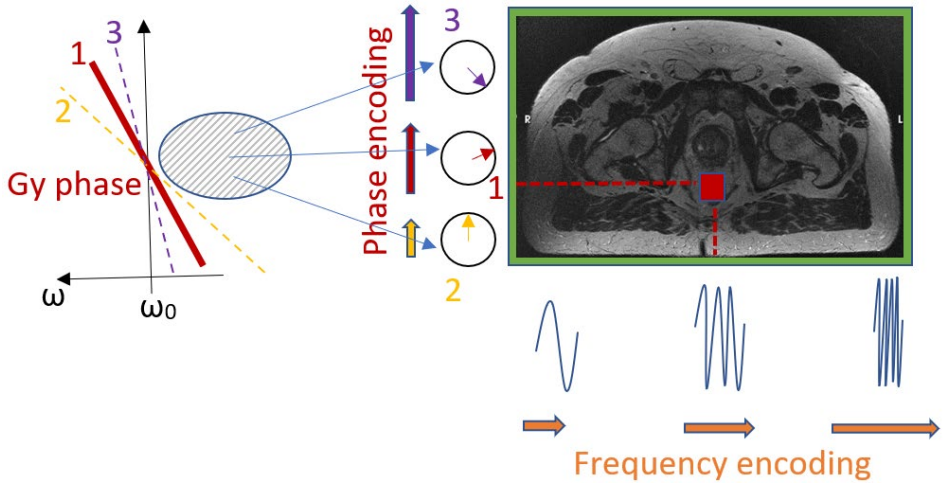

Figure 11. Gy is applied three times 1,2,3, and the different phases after Gy are turned off are shown in the circles. Phase encoding gradient is altered, and one resolution step is achieved for each gradient (1,2,3, ...). That is why phase encoding takes a long time, with one measurement per resolution level. Now each voxel in the image is uniquely identified in frequency and phase.

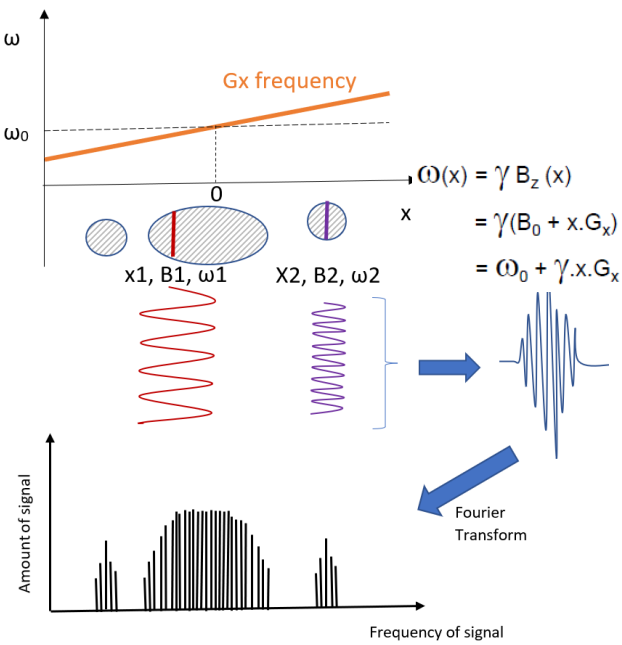

Figure 12. The principle of frequency coding. A combination of Gy and Gx and frequency analysis of the measured signal. One measured signal per slice and resolution level. The measured signal is digitalised and separated into discrete frequencies with the Fourier transform.

Pulse sequences, the image creation

To create an MR image, the signal measurement and the different gradients must be applied in a structured order, so-called pulse sequences. Depending on the pulse sequence, different contrasts are achieved, such as T1w, T2w, proton density, and diffusion.

There are two major MRI sequence groups, spin echo (SE) and gradient echo (GRE), with many alterations. Figure 13 shows a SE pulse sequence. The 90° RF will tip the net magnetization 90° to the xy-plane, and free induction will start immediately. The 90° RF is applied at the same time as the slice gradient Gz; subsequently, the frequency and the first phase coding gradients are turned on. After a delay time of TE/2 (TE, echo time), the 180° RF pulse is turned on. This RF corresponds to a B1 field applied along the x- or y-axis and will refocus the de-phased spins in the xy-plane. After another TE/2 time, the spins refocus, creating a detectible Mxy component. This procedure is repeated until the resolution level is accomplished, and the time between two repetitions is the repetition time (TR).

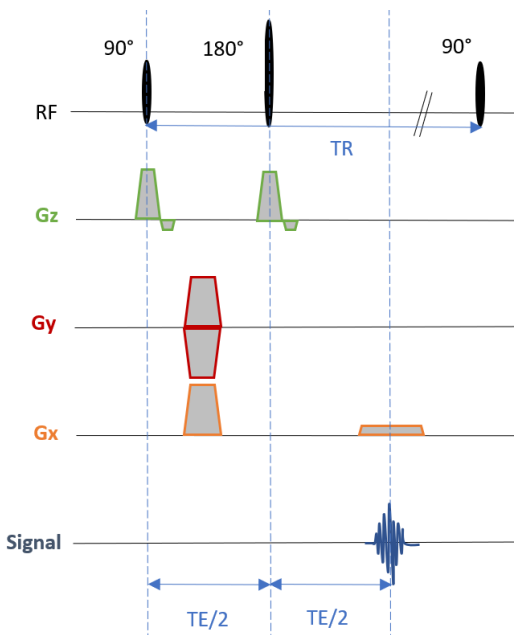

Figure 13. The spin–echo pulse sequence. A 90° RF pulse is applied together with the slice selection gradient, Gz. Subsequently, the first phase-encoding gradient is applied, followed by a 180°pulse. An echo is formed at echo time TE. The pulse sequence is repeated after repetition-time TR, but this time with a different phase-encoding gradient. When the sequence has been repeated for all phase-encoding gradients, the next slice can be imaged by repeating all phase-encoding steps for another slice-selection gradient.

If TR is long enough, all net magnetisation will have time to recover; however, if TR is short, only a fraction of the net magnetisation will be available for the next RF pulse. The relaxation rate depends on the T1 properties, and the T1 contrast (T1w) is created by choosing the TR. In an image, tissues with a long T1, such as Cerebrospinal fluid (CSF), will appear darker in an image than tissues with a shorter T1 (fat).

Similarly, we create T2 contrast (T2w) by adjusting the echo time, and the measured signal depends on the amount of magnetization still present in the transverse plane. Tissues with long relative T2 (prostate) will decay less until the 180° pulse, which yields a higher relative signal than tissues with shorter T2 (muscle). If there are long TE and long TR, the image contrast will depend on the net magnetization, M0, in the transversal plane and reflect the tissue's proton density.

The other type of sequence is GRE. The major difference from SE is that a gradient replaces the 180° refocusing pulse. This difference allows for shorter TR and therefore faster imaging. The absence of a 180° pulse allows for field inhomogeneities to influence the image contrast [6, 31, 32].

From signal to image

The Fourier transform is used to convert a measured signal to an image. As described earlier, the proton's location is determined by its frequency and phase. The Fourier transform decomposes the measured signal into frequencies. The signal from SE (also valid for other sequences) is first digitalised. The amplitude, which is a function of time, is amplified and stored in a discrete matrix, k-space. In k-space, one line of data corresponds to the digitised MR signal at a particular phase encoding level. Every point in k-space contains information from the whole image —the information changes depending on the position in k-space. The information about the fine details is stored in the outer border of the k-space, and low contrast details are stored in the centre of the k-space. The position in k-space is directly related to the gradient across the object being imaged. By changing the gradient over time, the k-space data are sampled in a trajectory through Fourier space. The number of phase coding steps depends on the desired resolution in the image. With the inverse Fourier transform from the frequency domain to the spatial image domain, the MR image can be visualised.

Magnetic resonance imaging in Prostate Cancer

To identify tumour volumes, American College of Radiology introduced Prostate Imaging – Reporting and Data System (PI-RADS v2.1) [7] to localise and grade PCa depending on site, location, and extent. PI-RADS includes T1w, T2w, diffusion-weighted (DWI), and gadolinium (Gd) dynamic contrast-enhanced (DCE) sequences, although DCE has a minor part in newer versions of PI-RADS

[7]. MRI is quite time-consuming. A PCa examination, according to PI-RADS, takes about 30 minutes in scan time.

T1w and T2w imaging
T1w images are used primarily to determine the presence of haemorrhage within the prostate and seminal vesicles and to delineate the outline of the gland. T2w images are used to discern zonal prostatic anatomy, assess gland abnormalities, and evaluate for seminal vesicle invasion and nodal involvement. See Figure 14 for examples of T1w and T2w images.

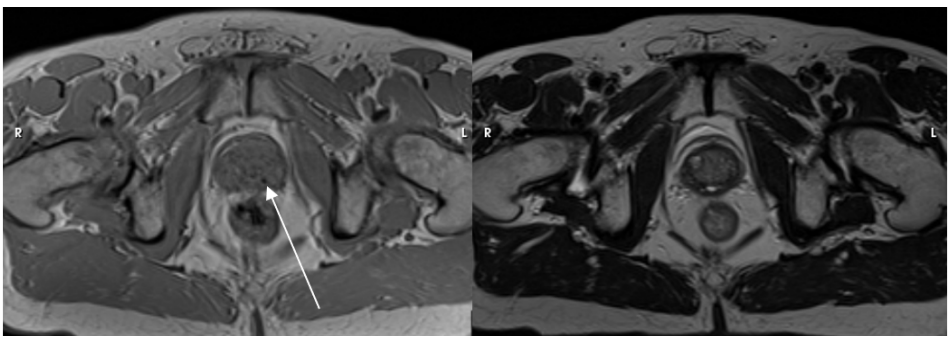

Figure 14. Examples of prostate images using T1w (left) and T2w (right). Images are produced for TP. In the left image, a dark fiducial marker is visualised (arrow), but the fiducial is not visible in T2w. Images from PARAPLY study.

Recently, more efforts have been made to acquire a quantifiable T2 map, where several images must be obtained with variable TE. The different images are then fitted into equation (3) and a quantifiable T2 parameter map is created. Quantifiable maps are efficient when the segmentation/identification of different tissues is needed. One study showed quantitative T2 values for PCa of 105 ± 28 ms, and these were significantly lower than benign peripheral zone tissue T2 values of 211 ± 71 ms [35]. In clinical practice, quantifiable T2 maps are not widely used.

Diffusion imaging
Diffusion-weighted MRI measures water mobility in the tissue and correlates with cellularity [9]. DWI is quantified with an apparent diffusion coefficient (ADC) map. Highly cellular areas such as tumours show restricted diffusion and appear as hypointense regions in the ADC [36, 37]. As a result, DWI is sensitive to microstructural tissue properties, including cell density, cellular organisation, and cell membrane integrity [37].

To measure diffusion [38], diffusion gradients must be added to, for example, SE sequence [6, 32], and the diffusion gradient creates a phase shift for moving water molecules. In figure 15 b, the water stands still, and all signal is recovered after the second gradient. If the water were moving (Figure 15 c) a lower signal would be measured.

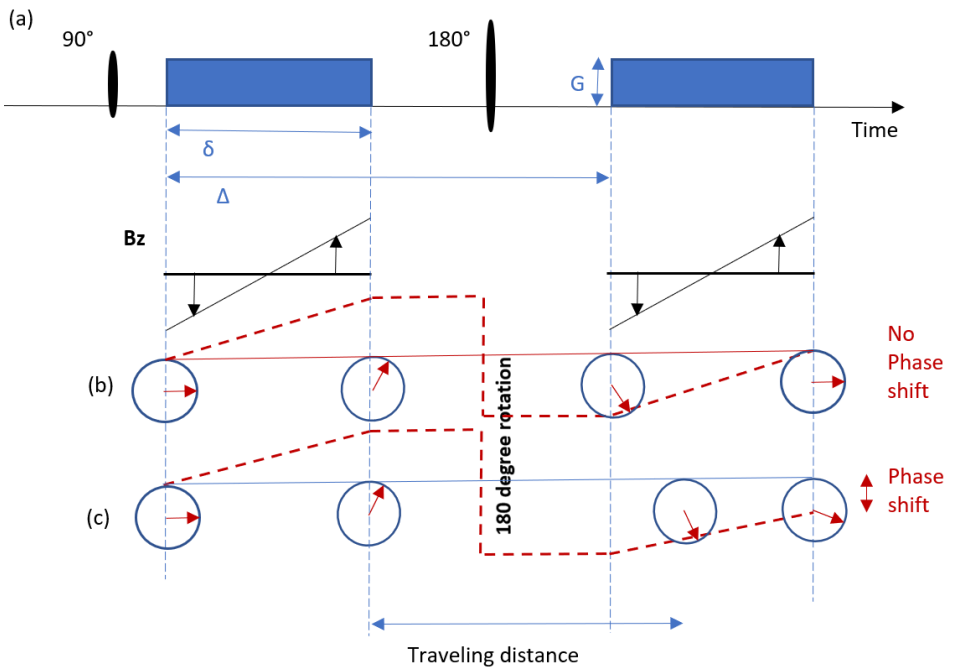

Figure 15. (a) Schematic diagram of the SE DWI pulse sequence. (b) Stationary water. The phase evolution of the spins (red-dotted line). Note that the 180-degree pulse inverts the phase wrap imposed by the first gradient pulse. The second gradient pulse, which is now identical to the first one in amplitude and length, completely refocuses this phase wrap. Stationary water implies a high signal in DWI. (c) Moving water. The phase evolution of the spins (red-dotted line). The spins have travelled between the gradient pulses and experienced different dephasing from the second gradient. A phase shift is created, and a lower signal is measured.

The signal from diffusion depends on the diffusion constant for the tissue but also on the diffusion sensitisation factor (b-value):

$$S(b_2) = S(b_1)e^{-b_2 D} \rightarrow D = -\frac{\ln\left(\frac{S(b2)}{S(b_1)}\right)}{b_2} \quad \text{where D = ADC in MRI} \quad [mm^2/s] \quad (4)$$

S = Signal from a particular b-value

D = self-diffusion constant

ADC = apparent diffusion coefficient.

D is the self-diffusion constant for the tissue, and a high self-diffusion means high motion and, therefore, a low signal on DWI. ADC is defined as the average area occupied by a water molecule per unit time (in mm²/s) and can be calculated using equation (4) (Figure 16).

The b-value in a SE depends on gradient amplitude (G), gradient duration (δ) and the separation between the diffusion gradient pulses (Δ), see figure 15.

$$b = \gamma^2 G^2 \delta^2 \left(\Delta - {}^{\delta}/_{3}\right) \quad \left[{}^{s}/_{mm^2}\right] \quad (5)$$

In DWI, a large gradient amplitude is needed, over 30 mT/m, to minimise the timing parameters for the diffusion gradients, thus avoiding long TE values [6]. In PCa, a minimum of two b-values are recommended for ADC, with the lowest over 50 s/mm² and the second around 1000 s/mm² also, a higher b-value of 1500 can either be measured or calculated but shall not be used for ADC map calculation due to (often) very low signal and noisy images [7].

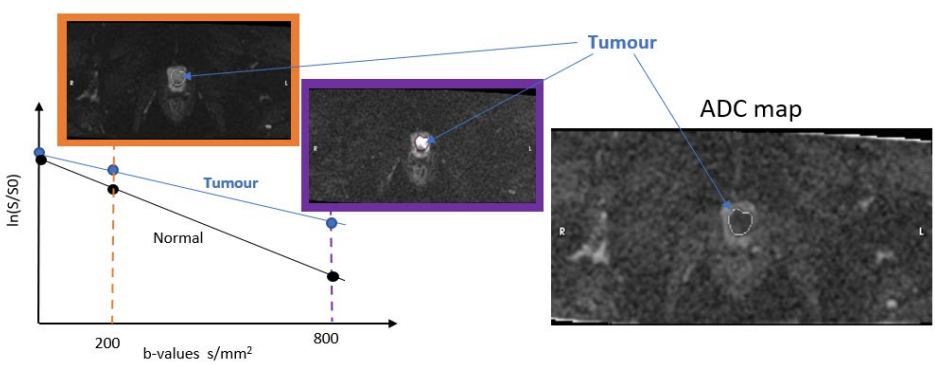

Figure 16. A simplified schematic graph over ADC calculation. The slope of the line, fitted through relative signal points, is the ADC. Here ADC is based on b1=200 and b2= 800 s/mm². Tumours have a higher signal than normal tissue in DWI and, therefore, a low ADC. Images from PARAPLY study.

DWI requires a fast signal acquisition with an echo planar imaging (EPI) sequence that fills the complete k-space in one acquisition. This is accomplished by multiple gradient reversals producing multiple gradient echoes during one T2* decay. EPI is sensitive to susceptibility artefacts in the transition between air and tissue and is present in the phase encoding direction. Although ADC is quantifiable, differences may occur depending on the vendor and the configuration of the diffusion gradients resulting in b-values. Furthermore, DWI is very sensitive to susceptibility differences between air and tissue. These differences can result in a distorted and geometric inaccurate image [39] and can lead to obstructed lesions [40]. ADC may be used for differentiation between benign and malign prostatic lesions with a threshold of 0.75–0.90 x 10^{-3} mm^2/s [7] and ADC values below the threshold correlating with clinically significant cancers [7].

Dynamic contrast-enhanced imaging

DCE is defined as the acquisition of rapid T1w GRE before, during, and after the intravenous administration of a Gd-based contrast agent. DCE is interesting because tumours differ from normal tissue, including having a higher proportion of leaking vessels. DCE continuously measures blood vessel wall leakage from the intravascular to extravascular space by imaging the inflow of the injected Gd in the tissue [41] and can be quantified and visualised as a kinetic parameter, Ktrans [41]. However, the actual kinetics of prostate cancer enhancement is quite variable and heterogeneous. Currently, the added value of DCE is not firmly established [7].

MRI after hormone therapy

Hormone therapy (androgen deprivation therapy (ADT)) influences prostate properties. Histopathological analyses by Reuter et al. [42] indicate that ADT affects PCa tissue, resulting in a 'loss of glandular architecture, cytoplasmic clearing, nuclear pyknosis, cytoplasmic vacuolization and mucinous degeneration'. These histopathological changes should generally allow for increased diffusion after ADT. ADT is also known to cause devascularization in both tumorous and benign prostatic tissue [43]. In paper II, we investigated the image statistics before and after ADT for ADC and DCE (Ktrans). The tumour characteristics were significantly altered after ADT with limited contrast with surrounding tissue. We found that ADC increased significantly after ADT, and the normal tissue ADC decreased significantly after ADT, which is in line with other studies [43, 44].

CT, basic principles and applications

For detecting PCa LN metastases and as input in the treatment planning system (TPS), CT is the primary choice of imaging modality. CT is based on X-rays passing through the patient and collected by a detector array [31]. The X-ray tube rotates around the patient, resulting in one photon attenuation map per angle with the corresponding tissue attenuation at that angle (linear attenuation coefficient μ/cm^{-1}). The intensity values of the beam on the different detectors will be the result of the attenuation process linked to the attenuation coefficients of the materials constituting the individual voxels. Hundreds of attenuation profiles are reconstructed (filtered back projection, iterative, or combination) into an image set. The matrix of the reconstructed attenuation maps is converted to a scale that expresses the attenuation coefficient for each tissue relative to the attenuation for water. This scale, the Hounsfield units (HU) scale, is defined as one change in HU, which corresponds to a 0.1% difference in the attenuation coefficient difference of water:

$$HU = (\mu_{material} - \mu_{water})/\mu_{water} * 1000 \qquad (6)$$

μ = attenuation coefficient

Attenuation coefficients are energy independent for air and water and set to fixed values in the HU scale; the HU of air is -1000 , because μ_{air} is approximately zero, and HU_{water}= 0 [31].

PCa imaging in CT

CT imaging is the preferred method for detecting metastases and for visualising bones (Figure 1). The imaging is fast and can cover a large volume in a few seconds. The drawback is the radiation exposure to the patient and poor soft tissue contrast. For tumour and LN metastases detection, a contrast media is injected intra-venously, and tumours with different vascularisation than normal tissue will be visualised as contrast-enhanced structures in the CT images.

PET/CT, basic principles and applications

PET imaging [31] is used to visualise the distribution of positron emitters (β^+-decay) marked on a carrier molecule, a radiotracer [45]. In the carrier molecule, an atom is replaced with a radionuclide emitting positrons. The carrier molecule corresponds to a specific biological function such as glucose consumed by the cells [46]. With higher glucose consumption, a larger amount of the radiotracer is used, and more positions are emitted from that location. Floro-deoxy-glycose

(FDG), with a flourine-18 (^{18}F) positron emitter, is widely used to image glucose metabolism.

The positron emission is imaged indirectly as the result of a positron-electron collision [31]. Within a few millimetres, the positron emitted from the radiotracer is close to coming to rest and combines with a free electron in an annihilation reaction. For ^{18}F, 75% of the annihilations in water occur within 1.2 mm from emission. This annihilation results in two 511 keV photons travelling at almost 180° angles from each other. These photons are detected by the PET detector ring (Figure 17). However, this angle comes with a small bit of uncertainty due to the positron's and electron's momentum and its conservation. This angular uncertainty results in a spatial resolution limitation of 2.5–3 mm for a 90-cm diameter scanner.

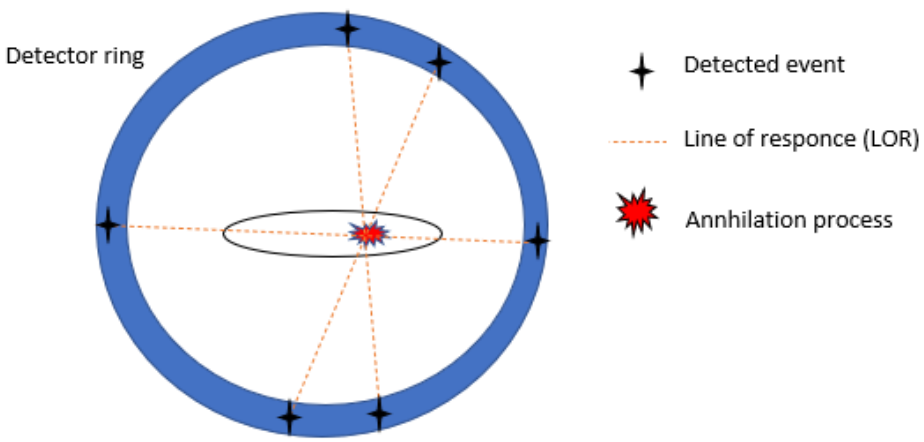

Figure 17. Schematic overview of PET functionality with LOR presentation. Annihilation process with photon registration in the detector ring.

The annihilation photons are assumed to originate from the same annihilation if the detections of the photons are within a small timeframe; the detection time window is typically approximately 10 ns. This type of event is called a coincidence event. PET techniques assume that detectors that register the same event (registration within the time window) can be connected with a straight line of response (LOR) or coincidence line (Figure 17). By registering several LORs, the distribution of the radiotracer can be calculated. However, all photons do not reach the detector ring. Photons can also be attenuated within the body or scattered; both effects can be corrected for [31, 47]. Attenuation can be corrected for with CT performed at the same time as PET. All modern PET scanners combine a PET detector ring and a rotating X-ray source with an accompanying

detector. Scattered photons are sorted according to the time window. CT contributes to localising the uptake of the tracer as well as for attenuation corrections.

PCa imaging in PET

PET provides functional information depending on the tracer used. A PET/CT examination takes up to an hour, including administering the radiotracer. The PET tracer ^{11}C-acetate (ACE) visualises fatty acid metabolism in the cell membrane [48, 49], which is often increased in PCa cells. ACE-PET is sparsely used for local disease and the results are diverse. One study showed increasing ACE uptake with age in the normal prostate and difficulty distinguishing cancer and benign prostatic hyperplasia [50].

Tracer uptake in PET images can be quantified with a standardised uptake value (SUV) in a region of interest (ROI) [51, 52] and calculated as follows:

$$\mathrm{SUV} = \frac{\text{Activity concentration in a ROI}}{\text{Decay corrected injected dose} / \text{patient weight}} \quad \left[{}^{g}/_{ml} \right] \qquad (7)$$

The ROI contains all visually increased pathological uptake with 42% $\mathrm{SUV_{max}}$ delineation threshold and enclose the functional tumour volume (FTV). In FTV the maximum SUV ($\mathrm{SUV_{max}}$) and mean SUV ($\mathrm{SUV_{mean}}$) are commonly used to describe the tracer uptake. For ACE uptake, the total lipogenic activity (TLA) can be calculated as follows:

$$\mathrm{TLA_{max}} = \mathrm{SUV_{max}} \mathrm{FTV} \ [\mathrm{g}] \qquad (8)$$

Acetate is replaced in the clinic by a tracer targeting the prostate-specific membrane antigen. PSMA is a transmembrane glycoprotein highly expressed in prostate cancer cells [53]. In benign tissues, the PSMA levels are low; in PCa cells, PSMA levels are high [53, 54]. PSMA can be radiolabelled to both ^{68}Ga and ^{18}F to make them more accessible as these radioisotopes have a longer half-lives than ^{11}C: ^{68}Ga has a half-life of 68 minutes, ^{18}F has a half-life of 110 minutes, and ^{11}C has a half-life of 20 minutes [45].

PET Imaging after ADT

ADT affects the tumour appearance in diagnostic MRI with a decreased prostate cancer conspicuity [43, 44]. However, the influence of ADT in ACE-PET is not clear. A study of mouse xenografts [55] suggests that ACE uptake is not affected by ADT. In humans, the effect of ADT on PCa appearance is still under evaluation.

For PSMA, the ADT influence seems to differ depending on ADT duration. Short-term (6 months) ADT seems to enhance the intensity of pathological PSMA

expression, whereas long-term ADT (3 years) reduces the tracer uptake. The treatment might influence PSMA uptake in long-term ADT [53].

External radiotherapy

External beam radiotherapy is a standard treatment for PCa where the radiation is delivered from a linear accelerator (linac). Today, linacs usually use volumetric modulated arc therapy (VMAT), where the radiation is delivered continuously in a rotating arc around the patient. During VMAT treatment, the radiation is also modulated to achieve highly conformal dose distributions with precise planning target volume coverage, resulting in minimal irradiation of healthy surrounding tissue.

Images for treatment planning

CT and/or MRI imaging are used for individualised treatment planning (TP). The CT/MRI used for TP must be achieved with the same patient geometry as achieved at the linac. This includes knee support, a flat tabletop, and fiducial markers implanted in the prostate for image guidance at the linac and as registration points between CT and MRI if used.

In a CT-based workflow, MRI is often used for delineating organs at risk (OAR) and tumour targets as MRI has better soft tissue contrast than CT. In this workflow, CT and MRI are co-registered in the TPS with the fiducial markers as registration structures. The TPS uses the attenuation information from CT for the dose distribution calculation to the different targets. The relationship between electron density and CT number in the TPS needs to be established by a calibration procedure. In the calibration process, the relationship between HU CT numbers and the type of density (either mass and/or electron) is determined through a tissue surrogate phantom [56]. The calibration factor is implemented in a look-up table in the TPS and generates electron density maps from CT-based HU images used for the dose calculations.

In an MRI-only workflow, CT is not performed, but a synthetic CT (sCT) is created from MRI scans [57-59]. In sCT, an electron density map is calculated from MRI and replaces the HU-based CT used in TP [58]. sCT is commonly determined either via an atlas-based or a voxel-based approach. In short, an atlas-based approach is a single, standard MRI sequence deformable registered to a standardised anatomical CT atlas [58]. Voxel-based aproaches uses MRI intensities from several sequences to assign tissues with electronic density information [58]. Replacing CT with an sCT introduces less than a 0.5–1% dosimetric difference between TPs and is considered acceptable [57, 58].

Images used in the diagnosing process of PCa can be used in the TP process but with some limitations. Diagnostic images, preformed before hormone therapy,

still have the tumour contrast intact, but these images are rendered without specific geometry – i.e., not using a flat tabletop, knee support, and fiducial markers. In addition, these images are not always imported to the TPS and used only as visual guidance for the intraprostatic target.

Target definitions

In treatment planning, OAR and treatment targets are delineated. These targets, defined by an oncologist according to the criteria in ICRU 50 and 62 reports, are gross tumour volume (GTV), clinical target volume (CTV), and planning target volume (PTV) [60, 61].

The GTV may include the dominant intra-prostatic lesion and malignant LNs. GTV is based on available images and clinical information (TNM classification), including previous CT, MRI, and PET images. Outlining GTV comes with several uncertainties, mainly as a result of image quality and manual outlining [62]. The CTV is defined as GTV with the addition of a margin tissue with potential microscopic disease not visible on medical images. In PCa, the whole prostate gland is considered CTV, and the introduced uncertainties are again the result of poor image quality and manual outlining. To compensate for target movements and geometrical uncertainties, a margin is added to CTV, which results in PTV. There have been suggestions for margin recipes for PTV that consider all types of errors [63]. Errors overall disturb the dose distribution. Random errors such as daily variations in patient set-up blur the cumulative dose distribution, whereas systematic errors due to treatment preparation (outlining, CT to MRI registration, etc.) shift the dose distribution relative to the target [63]. The most pronounced contribution to PTV dose uncertainty is setup errors and intra-treatment organ motion, which lead to day-to-day variations. The PTV margins used at Norrlands Universitetssjukhus (NUS) are summarised in Table 5 and visualized in Figure 18.

Table 5. Volume specifications in high-risk/very high-risk PCa with WPRT at NUS. Fiducial markers and CT-based TP with MRI co-registration to outline target and OAR.

	Target	Dose /Gy (fractions)	Added margin/ mm
GTVT	Dominant intra prostatic lesion	84 (35)	4
GTVN	Positive LN nodule	70 (35)	7
CTVT1	Prostate	77 (35)	7
CTVT2	Vesicles	56 (35)	7
CTVN	LNs in the pelvis, including vesicles	56 (35)	8

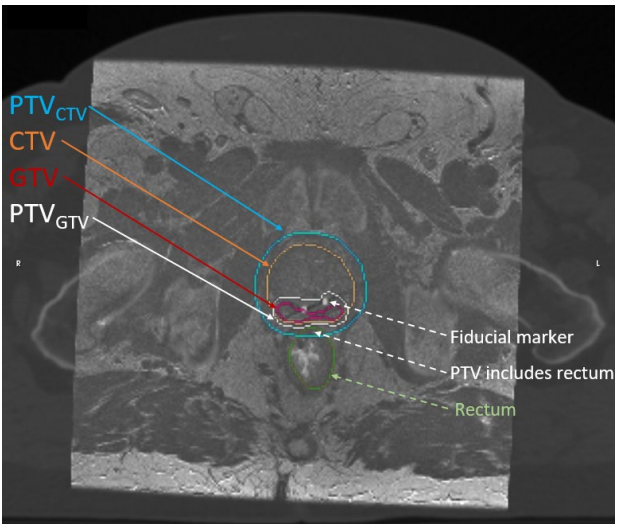

Figure 18. Images from TP. CT with a fiducial marker registered MRI T2w with a smaller field of view as an overlay. PTV, CTV and GTV are outlined in MRI. For this patient, PTV includes parts of the rectum.

CT-based TP includes MRI because MRI provides better soft tissue contrast than CT. MRI contributes to defining not only CTV and GTV but also OAR outlining [64]. The drawback is the registration uncertainty between CT and MRI, but this can be minimised with fiducial marker registration. Fiducial-based CT to MRI registration for the prostate can lead to spatial deviations up to 2 mm in the TP [65]. If TP were based on only sCT calculated from MRI, the PTV could theoretically be reduced by 2 mm. In CT-based RT, CTV-PTV margin is generally 5–8 mm, including registration uncertainties, organ movement, set-up, and mechanical uncertainties [66].

Treatment alternatives in PCa

Depending on the risk classification of PCa, the treatment decision can be active (monitoring) surveillance for PCa graded as risks classified as 1–2, radiotherapy, or radical prostatectomy for risks 3–5. When PCa is limited to the prostate, it is considered localised and potentially curable [67]. For high-risk or very high-risk PCa (risk 4 or 5), ADT is combined with radiotherapy or radical prostatectomy, and the treatment choice depends on T classification [2]. In radiotherapy, ADT works as a radiosensitiser [68] and reduces prostate volume [43, 44, 69]. If metastases is present, the treatment mainly focuses on quality of life with life-prolonging intent [67, 70]. However, treatment options are available, such as

hormonal treatment, chemotherapy, and external beam radiotherapy, but not with curable intent [2].

Treatment strategies for high-risk and very high-risk PCa

The Swedish recommendations for high-risk (HR) and very high-risk (VHR) PCa suggest several RT strategies in combination with ADT [2]. The recommendations for HR/VHR PCa cover prostate and LN targets, boosting to the dominant intraprostatic lesion (DIL), fiducial markers, and using perirectal spacers.

Androgen deprivation therapy

Because the prostate gland requires androgen to function optimally, hormonal therapy (testosterone deprivation) can be very effective. ADT reduces androgen levels and therefore reduces or stops PCa cell growth, resulting in shrinking PCa cells [43, 44, 69] or slowing PCa cell growth. However, ADT alone does not cure PCa. ADT makes androgen receptor-expressing PCa cells more vulnerable to radiation and significantly improves overall survival when RT is combined with ADT [68, 71]. ADT is given both neoadjuvant and adjuvant, and an extended adjuvant ADT period correlates well with improved progression-free survival [72] in combination with RT and neoadjuvant ADT.

Radiotherapy strategies

The RT strategies depend on PCa risk classifications. The recommended RT in high-risk cancer is either ultra-hypofractionated treatment with a total dose of 42.7 Gy in 7 fractions [2, 73] or hypofractionated treatment with 60 Gy in 20 fractions [2]. Hypofractionated treatment can be dose escalated up to 66 Gy. At very high risk, 78 Gy in 39 fractions is recommended. Furthermore, at T3b, the seminal vesicles should be included in CTV according to Swedish recommendations [2].

Concomitant radiotherapy to the pelvic LNs (WPRT) as a prophylactic treatment has been discussed for a long time. The intent is to prevent micronodular metastases from developing not yet visible with diagnostic imaging techniques such as MRI and PET/CT. WPRT with a total dose of 50 Gy in 25 fractions may be considered for men with cancer categorised high or very high risk without or with a few detected regional LN metastases with PSMA-PET/CT [2]. If PCa is classified as N1, the typical approach is palliative ADT and not WPRT, but the recommendations are under consideration in Sweden. A recent study (POP-III) has shown that WPRT is safe and improves biochemical failure-free and disease-free survival compared to the prostate only as a target [74]. Disease-free survival after five years was 90% in the group receiving radiotherapy to the pelvic LNs and 77% in those who received radiotherapy to the prostate alone [74]. WPRT fractionation is, in most cases, between 44 and 50 Gy in equivalent doses in 2 Gy

fractions (EQD-2) to pelvic nodes, including the common iliac and 64–78 Gy to the prostate target with EQD-2 [75].

Focal Boosting

External focal boost radiotherapy may be considered in cancer with high or very high risk and when a corresponding lesion is detected on MRI [2]. A well-defined and precise RT is key to successful treatment. Studies have shown that local recurrences often appear at or close to a dominant prostatic lesion [3, 4]. Therefore, it has been suggested that tumour volumes within the prostate should be targeted with dose escalation and boosting [2]. A review from 2016 [76] reports that RT can be used to boost the whole prostate, and most patients can tolerate a radiation dose (EQD2) ≤ 86 Gy to the whole prostate. However, a larger DIL boost is preferable, and many studies use a boost dose to the DIL of (EQD2) > 90 Gy [76], and dose escalation to the DIL seems to be favourable. Recent published DIL boosting data (FLAME) [77] have shown the technique to be safe and superior for tumour control compared to traditional non-DIL boosting PCa RT treatment. Figure 19 shows a dose distribution for WPRT with boosting to the prostate and LN.

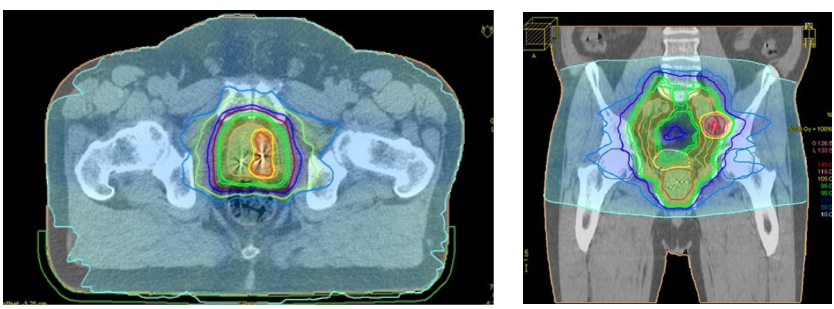

Figure 19. Treatment planning with iso-doses and boost volume to GTV prostate (left) and GTV-LN (right). Images from PARAPLY study.

Fiducial Markers in RT

External beam radiotherapy of prostate cancer relies on precise knowledge of the prostate location at treatment. The national recommendation for PCa treatments in Sweden is that treatment planning should be based on CT or MRT after the prostate's fiducial markers are implanted [2] (Figure 17).

Fiducial markers are essential to guide PCa treatment due to prostate movements [78-80]. Fiducials are used to minimise the treatment margins to CTV due to motions and are visualised with the X-ray/Conebeam CT on the treatment machine. Fiducials are necessary due to the poor soft tissue contrast where prostate images produced at the treatment machine are not satisfactory for

image-guided radiotherapy. Fiducials are used both as treatment guidance and for image registration between CT and MRI when creating treatment plans (Figure 18). For prostate cancer with LN involvement, CTV includes both the prostate and LNs in the pelvic area [27, 81-83].

Perirectal Spacer in RT

Some clinical studies suggest using a perirectal spacer for patients with an increased risk of rectal side effects [2]. Rectal side effects are common after PCa radiotherapy. A higher radiation dose to the prostate can improve biochemical outcome, but dose escalation significantly increases the risk of treatment toxicity [84]. It is important that appropriate margins are applied – i.e., margins that are large enough for successful treatment and small enough to minimise radiation exposure to healthy tissue and minimise side effects. The anterior rectal wall is particularly vulnerable due to its anatomical proximity to the prostate. Consequently, rectal complications are frequent, including loose stool, frequent defecation, urgency, rectal discharge or bleeding, and impaired QoL [17]. To reduce the rectal dose, a spacer can be inserted between the prostate and the anterior rectal wall to separate the rectum from the prostate (Figure 20). Prada et al. 2007 [85] conducted the first study using hyaluronic acid (HA) as a perirectal spacer; this study has been followed by multiple studies with several different agents acting as spacers [86]. These studies suggest that spacers reduce the rectal dose and subsequently late toxicity [87]. The quality, placement, and thickness of the spacer are essential [88] and can influence rectum doses [88-90]. Despite many studies on perirectal spacers, most studies are small and lack long-term follow-up [87]. As a result, the impact on quality of life and cost-effectiveness have been questioned, and the use of spacers in the clinic has not been universally accepted.

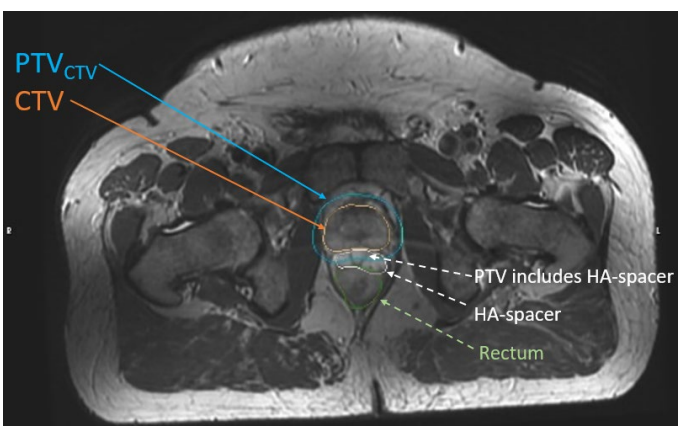

Figure 20. HA-spacer pushing rectum away from PTV. PTV does not include the rectum. T2w MRI was used for TP from the NOHARM study.

Methods

MRI has excellent soft tissue contrast, but tumour properties such as cellularity in ADC maps can be visualised and measured. MRI is used in all included papers, and the MRIs are often repetitive within a few weeks period. To analyse target volume changes in time, a registration technique that considers organ movement and volume change are central. All image analyses were done in MICE Toolkit (Nonpi Medical AB, Umeå, Sweden). MICE Toolkit uses a visual programming interface and includes the open-source software Elastix [91], which consists of image manipulation and registration algorithms. The studies' datasets and analysis are summarised in Table 6 and further described in the text.

Table 6. Overview of study populations and methods.

	Dataset	Approach	Analysis
Paper I	10 patients from MOVE. MRI (T2w) on six occasions during the RT process	Movement measurements of LNs and prostate during RT	Deformable image registration with anatomical landmarks as reference
Imaging	Siemens: T2 SPACE: TR/TE 2000/133 ms; 176 slices; FOV 300 mm, voxel 1.2×1.2×1.0 mm^3 GE:T2 CUBE: TR/TE 1240/103 ms; 196 slices; FOV 320 mm, voxel size 0.81x0.81x1.0 mm^3		
Paper II	50 patients from PARAPLY MRI (T2w, ADC, Ktrans) before and after ADT	Can texture analysis improve tumour detectability after ADT?	Contour propagation with DIR from baseline to images after ADT
Imaging	T2w, TE=97.6 ms, TR=9873 ms, matrix: 512 x 512 x 52, voxel: 0.5 x 0.5 x 2mm^3, no gap DWI Focus, TE=69.4 ms, TR=3500 ms, matrix: 256 x256x16, voxel:0.9x0.9x4mm^3, 4 average, b-values: 200 s/mm^{-2} and 800 s/mm^{-2} Fast SPGR+Gd, TE=1.88 ms, TR=4.36 ms, matrix: 256x256x12, voxel: 1x1x 5mm^3, mean temporal resolution 11.3 s, Dotarem 0.2 ml/kg		
Paper III	52 patients from NOHARM. MRI (T2w) before and three sessions after HA	HAspacer: its stability and influence on rectum dosimetry	HA stability evaluation with DIR and dosimetric impact during RT
Imaging	T2w, TE=115 ms, TR=15670 ms, matrix: 256 x 256x 57 voxel: 1.2 x 1.2x3.6 mm^3, 3 averages, no gap		
Paper IV	76 patients from PARAPLY. Acetate-PET-CT and MRI ADC imaging before RT	ADC and Acetate uptake in GTV and correlation to progression	Descriptive statistics
Imaging	DWI: TE=69.4 ms, TR=3500 ms, matrix: 256x256x16, voxel: 0.9x0.9x4mm^3, 4 average, b: 200 s/mm^{-2} and 800 s/mm^{-2} **or** TE=87 ms, TR=4000 ms, matrix: 160x136x20, voxel:1.6x1.6x3.6mm^3 b: 0 and 800 s/mm^{-2} ACE-PET/CT: average activity 454 MBq, time-of-flight mode with 2 min/bed position, from the proximal femur to the head.		

Contour propagation

To follow a structure such as a target volume or an organ over a period of time using repetitive imaging requires an image registration method. A method for following structures in the pelvic region can be a two-step registration workflow starting with a rigid registration followed by a deformable image registration.

When registering one image (moving image) to a baseline image (fixed image), several functions must be considered, such as similarity metric, transformation, optimizer, and interpolator [91-93]. The transformation type is often used to describe the type of registration (rigid (RR), affine, or deformable registrations (DIR)) even though a registration procedure contains more functions (Figure 21).

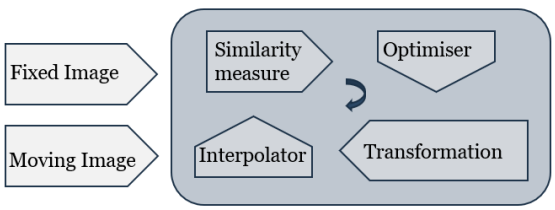

Figure 21. The similarity measure describes how much information the two images have in common. The optimisation algorithm tries to maximize the similarity between the two images by changing the deformation vector field, and the moving image is deformed with the appliance of the vector field. Then the workflow starts again by comparing the deformed moving image to the fixed Image.

The similarity metric [91, 92] relates the image intensities between fixed and moving images. Similarity metrics use cost functions that quantify the degree of similarity between two images and cost functions adjust the parameters of a spatial transformation model until the cost function reaches a local optimum. Mutual information, a similarity measure recommended for multimodal medical image registration, describes how much information two images have in common.

Different types of MRI sequences count as different modalities due to their large variation in tissue contrast between sequences. Mutual information can be considered a measure of image agreement between two images in feature space, not in the image domain. In feature space, the grey tone correspondence is presented as grey values from the fixed image on the x-axis and grey values from the moving image on the y-axis to form a joint histogram. When the images are correctly registered, the joint histogram will show clusters of grey tones of matching structures. The joint histogram counts how many times each grey tone correspondence occurs. If the fixed and the moving images were identical, the joint histogram would be presented as a straight line because the grey levels in the images are identical. The joint histogram is computed by setting the number of histogram bins, a number that depends on the image's dynamic range. Often,

32 is a good choice for the number of histogram bins, but some situations work better if 16 or 64 is chosen.

The optimiser [91, 92] maximizes the similarity measure. Optimization is an iterative process that is used to calculate the best registration estimate. For a rigid registration, 500 iterations work well; for more robustness in DIR, up to 2000 iterations is preferable, but the prolonged calculation time required for this many iterations is a drawback.

The transformation procedure [91, 92] defines the mapping between the two images. There are three basic types of transformations: rigid, affine, and deformable. Rigid image registration is global in nature and constrained to allow only 6 degrees of freedom – namely, translations in three orthogonal planes and rotations of pitch, yaw, and roll. Only the coordinate system will change in RR, not the image contents. Affine transformation, which is more comprehensive and accounts for global gross distortion, is achieved via three rotations, three translations, three stretches, and three shears. Here, the image registration will compensate for different scales and captures global image motions. Deformable (or nonrigid) image registration is non-global and allows for different local regions to be registered in different ways, mimicking the deformable nature of tissue. This is achieved by using b-spline curves defining a deformation vector field (DVF) that mathematically describes how voxels from one image are deformed so that they correspond to another image. In Figure 22, a vector field map is visualised with a fixed T2w image.

When registering two MRIs, a b-spline transformation of order 3 in the final step can be used. In a b-spline transformation, a grid of control points is used, which controls the transformation of the moving image. The control point spacing of the b-spline transformation in the finest resolution level can be 5–8 mm but adjusted if necessary. An error measure is used to measure the registration error between the moving and fixed image. However, if the first RR does not align the two images correctly, a DIR will not be possible, irrespective of parameter choice. A RR transformation should first be performed to manage a robust DIR transformation. A proper RR is essential for the DIR, which otherwise will quickly diverge, and this type of registration workflow was used in papers I–III.

Image processing

All images are processed in MICE, including the calculation of dose-volume histograms, ADC map, Ktrans, and image registrations. To follow pathology or a region by repeated imaging requires a registration method suitable for the included medical images and the purpose of the registration. The purpose can be volume of interest (VOI) propagation as in paper III, where the hyaluronic acid, CTV, and rectum were outlined in T2w MRI for TP. In the repetitive imaging, these VOIs were transferred via registration and contour propagation. Paper I,

focused on measuring LN movements during an RT course by using a series of T2w MRIs and demanded high DIR accuracy in large volumes surrounding the small LN. The LNs were also outlined in every MRI for quality assurance reasons. Paper II aimed to transfer the suspected tumour VOI from ADC MRI to DCE MRI. Next, the tumour VOIs were transferred to the MRIs taken three months after ADT started. This procedure includes contour propagation between image types and images with different contrast and pathology size due to ADT.

Movement analysis in the target volume

To measure the movements inside CTV, six repetitive MRIs were used (Table 6) and included ten patients diagnosed with PCa scheduled for treatment with image-guided radiotherapy (IGRT). The baseline MRI was performed on the same day as the treatment planning CT, and the five following MRIs after IGRT on treatment day 1, 3, 5, 20, and 35. For patients 1–5, a Siemens Magnetom Espree 1.5T was used; for patients 6–10, a GE Signa PET/MRT 3T was used. All scans were 3D-distortion corrected and performed with a flat tabletop and similar positioning as used during RT.

CTV was divided into sections, and a centre of mass point (COM) was created in each section (Figure 22). All MRIs were then registered to the baseline MRI with DIR, and the resulting vector field (Figure 22) from each registration gives the deviation from the baseline MRI. For quality assurance, we identified LNs in the baseline MRI for each patient and then identified the same LN in the following MRIs. For each MRI, the distance between COM (including lymph nodes) and the prostate were measured (Figure 22) along with the deviation from the baseline MRI.

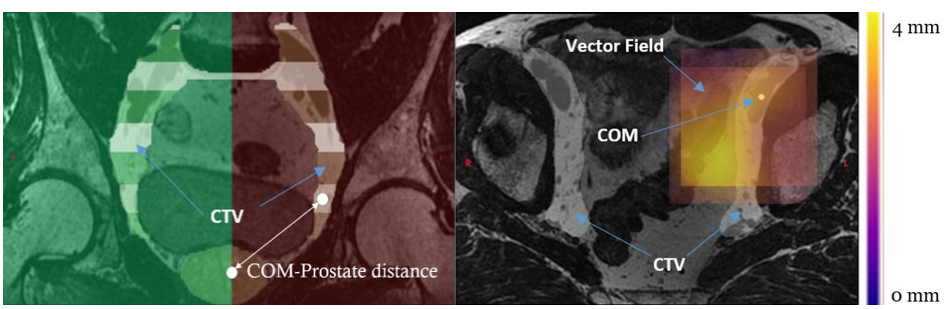

Figure 22. The COM, used for movement analysis, is shown inside CTV. CTV is divided into sections (left). The deformable vector field from the registration process (coloured) is centred around the COM (right). Deviation from baseline is 0-4 mm. Both images are T2w MRIs from the MOVE study.

Target imaging

To identify the DIL after ADT, we used contour propagation . In total, 50 patients were included (Table 6). All were scanned on PET/MRI (Signa 3T, General Electric medical system) and had ADC imaging before and after ADT. Of these, 39 had DCE before and after ADT. Imaging was approximately three months apart.

In the baseline ADC images, the DIL (Tumour VOI in Figure 23) was identified. Also, a reference VOI were outlined, representing normal prostatic tissue. After ADT, the imaging was repeated. DIR was used to propagate the Tumor VOI and the reference VOI to all other MRIs included in the evaluation, but the DWI (b-200 s/mm^{-2}) was used in DIR because of the image contrast and less noise than ADC.

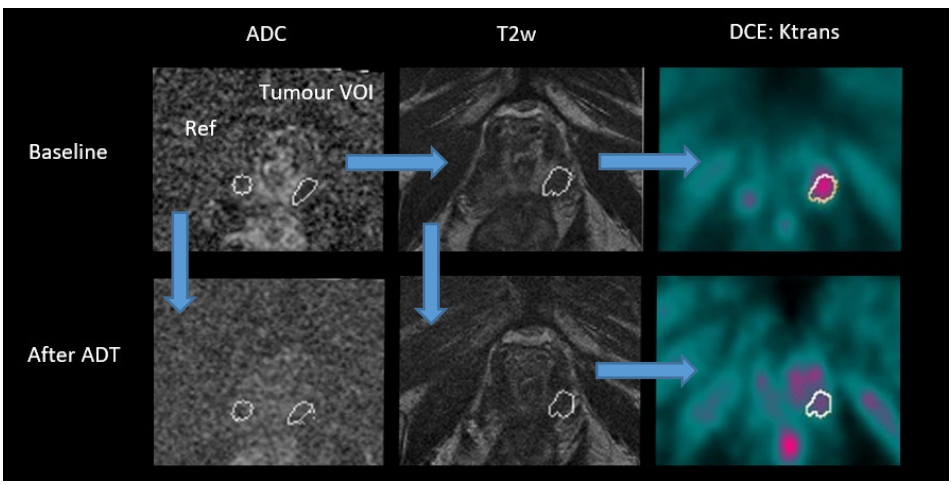

Figure 23. Tumour VOI and reference tissue identification in baseline ADC. These contours were propagated to all other images at baseline and after ADT. Blue arrows indicate the DIR order.

Target identification

To identify DIL after ADT, first-order statistics (mean, median etc.) and texture analysis in the tumour (DIL) and reference VOI was performed. For textural analysis, the grey-level co-occurrence matrix (GLCM) was used. GLCM is a method of examining image texture that considers the spatial relationship of pixels. GLCM is a function of both the angular relationship and distance between two neighbouring pixels [94]. Figure 24 illustrates how the Haralick texture

features are computed in a 4 x 4 image with three grey levels (1-3). The GLCM is constructed by considering the relation of each voxel with its neighbourhood. The Haralick texture features are functions of the normalized GLCM, where different aspects of the grey-level distribution in the image are represented. For example, diagonal elements in the GLCM represent voxel pairs with equal grey levels. The texture feature "contrast" gives elements with similar grey-level values a low weight and elements with dissimilar grey levels a high weight.

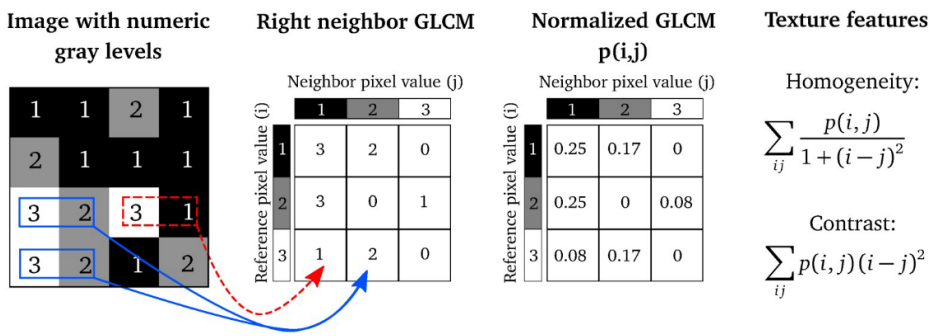

Figure 24. An illustration of how the Haralick texture features are computed in the horizontal direction. In this example, there are two instances when a reference voxel of 3 "co-occurs" with a neighbour voxel of 2 (solid blue line), and there is one instance of a reference voxel of 3 with a neighbour voxel of 1 (dashed red line). GLCM is then normalised, and from this normalised matrix, the texture features are calculated. Reprinted with kind permission from Löfstedt T, Brynolfsson P, Asklund T, Nyholm T, Garpebring A (2019) 'Gray-level invariant Haralick texture features'. PLoS ONE 14(2): e0212110. https://doi.org/10.1371/journal. pone.0212110 [94].

To summarize, GLCM functions characterise an image's texture by calculating how often pairs of pixels with specific values and in a specified spatial relationship occur in an image. When creating a GLCM and extracting statistical measures from this matrix, more information than meets the eye is possible to achieve. Radiomics strategies for PCa [95-99] are often based on GLCMs to separate or classify tissue.

In paper II, GLCMs were computed in MICE software in four directions (horizontal, vertical, and two diagonals) and separated for each slice. The GLCMs for the four directions were then combined and analysed as the mean GLCM. In the mean GLCM, invariant Haralick texture features [94, 100, 101] were calculated from the mean normalized GLCM. The invariant features are more robust and do not depend on the number of quantisation grey levels. The

invariant features and the original Haralick features describe, for example, the homogeneity and contrast among other features [94].

VOI differences (reference vs DIL before and after ADT) were analysed with Wilcoxon Signed Ranks Test for dependent samples with a Bonferroni correction yielding a significance level of $p < 0.0019$. Spearman's rank correlation coefficient was used for correlation tests between features.

Hyaluronic acid-spacer, stability and rectum dosimetry

Hyaluronic acid stability and influence on rectum doses were studied. In a single-centre phase II study, 52 patients were eligible for HA/dosimetry evaluation (Table 6). The patients received transrectal injections with HA as a spacer to separate the ventral rectal wall from the prostate.

MR scans were achieved before (MR0) and after (MR1/MR2/MR3) HA injection. The first MRI with an HA spacer (MR1) was used in treatment planning. The second MRI (MR2) was scanned in the middle of the RT, and MR3 was scanned at the end of the RT. Before 2015, an Espree 1.5 T MRT (Siemens) was used; after 2015, a Signa 3T PET/MRT (General Electric) was used. All scans were performed with a flat tabletop and similar positioning as during RT. Between CT and MR1 a fiducial registration was performed as a basis for TP.

In the TP images, the HA, CTV and rectum were outlined by an oncologist. The structures were then propagated to all other images with an RR+DIR workflow. MR0, MR2, and MR3 were then registered to MR1, and the dose matrix from TP could then be used for dosimetry analysis. Figure 25 shows representative T2w with HA as a white structure between the prostate and rectum on four occasions for one participant. The HA thickness and the space between CTV and rectum (CRS) were measured in MR0-4.

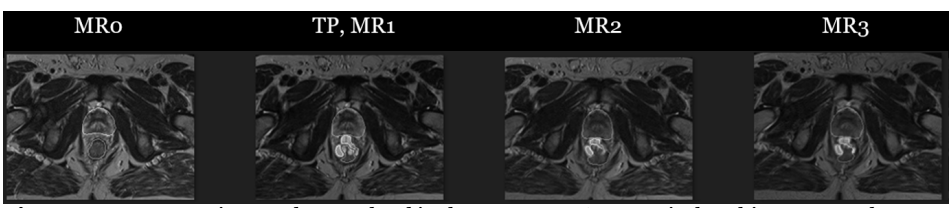

Figure 25. MRI over time, at the apex level in the prostate. HA-spacer is the white structure between the prostate and the rectum. T2w MRI from NOHARM study.

The Wilcoxon signed-rank test was used to compare rectum doses based on MR1 to rectum doses based on MR0, MR2, and MR3. The differences in volume and shape/thickness of the ROIs were also tested with Wilcoxon. The tests were two-sided and considered significant if $p<0.05$. Spearman's rank correlation coefficient test was performed to evaluate the thickness of HA compared to the

CRS with a significance level of $p<0.05$. Time to first late side-effect was calculated using the Kaplan-Meier method from the start of RT. All statistics were performed in SPSS v.28 and R-studio.

Pre-treatment imaging

Of the 76 patients included (Table 6) in the pre-treatment imaging analyses, 31 were retrospectively classified for the present analyses as HR and 45 as VHR PCa according to Swedish guidelines [2].

Baseline MRI and PET examinations were performed before ADT, approximately three months before the start of RT. MRI (Siemens Magnetom Espree 1.5T 2013-2014) or PET/MRI (Signa 3T, General Electric medical system, 2015-2017) was performed with a flat tabletop and the same fixation equipment as used during RT.

For the purposes of the image analyses only, the DILs were retrospectively outlined in the baseline images before ADT. The DIL in ADC is referred to as DIL^{ADC}, and the DIL in ACE-PET is referred to as DIL^{ACE}.

DIL^{ADC} was delineated by an oncologist (KS) for the participants included between 2013–2014. For the remaining participants, DIL^{ADC} was identified by two radiologists in consensus (LB and MS). The median ADC value in DIL^{ADC} was used in the evaluation, along with the volume of DIL^{ADC}.

In the PET/CT images, a nuclear medicine specialist (SS) defined uptake in ACE-PET images in the prostate. The total lesion lipogenic activity (TLA_{max}) was calculated in the functional tumour volume. The median TLA_{max} in DIL^{ACE} was used in the evaluation, along with the volume of DIL^{ACE}.

The Mann–Whitney U test was used to investigate differences in imaging parameters between different patient groups. This test was also used for the evaluation of ADC between different vendors. Spearman's correlation test was used to correlate DIL parameters, PSA, Gleason, N-stage and T-stage. All statistics were evaluated with $p<0.05$ as the significance level. All statistics were performed in SPSS v.28 and R-studio.

Results

The target volumes were analysed in several ways; margins due to motion (paper I), PTV proximity to the rectum (paper III), and DIL identification after ADT (paper II). Also, quantifiable image parameters in the DIL target volume were analysed in relation to oncological parameters and outcomes (paper IV). The study results are summarised in Table 7.

Table 7. Overview of study results.

Results	
Paper I	In some extreme cases, areas inside the CTV (LNs) were as mobile as the prostate and not fixed to the bones.
Paper II	After ADT, only ADC median value could significantly differentiate between tumour and reference tissue. Texture features did not contribute to differentiation.
Paper III	Significant reduction in the relative rectal volume reciving dose V70% (54.6 Gy) and V90% (70.2 Gy) between MR0 and MR1 as well as between MR0 and MR2 and MR3. HA thickness and CTV-rectum space increased between MR0 and MR1 but decreased from MR1 to MR2/MR3.
Paper IV	Acetate-PET: Progression: TLAmax = 112 [68.1-166.8] g No Progression: TLAmax = 84.7 [50.3-114.3] g ADC MRI: Progression: ADC=0.75 [0.70-0.83] x 10^{-3} mm^2/s No Progression: ADC = 0.74 [0.71-0.78] x 10^{-3} mm^2/s No oncological parameters were correlated to the median ADC.

Movement analysis in the target volume

We used DIR to evaluate interfractional movements of LN regions commonly included in the pelvic CTV for high-risk prostate cancer patients (paper I). Figure 26 shows the CTV subsections and the deviations from the baseline in each section. The distance between COM and prostate can be interpreted as LN movements in IGRT with a prostate registration technique.

The COM to prostate distance was measured. The deviation from the baseline in the right-left (R-L) direction was 1–4 mm, in anterior-posterior (A-P) 4–7 mm, and in cranio-caudal (C-C) 3–6 mm for 95% of the cases.

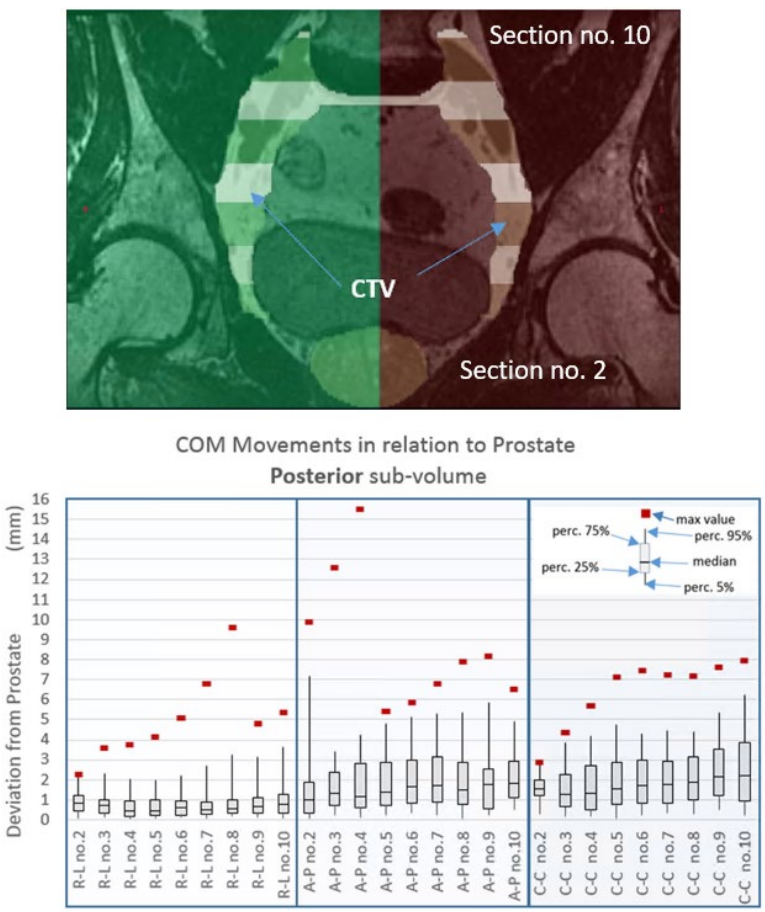

Figure 26. Posterior subsections of CTV are visualised in a T2w image from the MOVE study (top). The graph shows the distance between COM and prostate for each section and movement direction.

Target imaging

We used first-order statistics and texture analysis to identify intraprostatic tumour lesions after neoadjuvant androgen deprivation therapy (paper II).

The intra-prostatic lesion was outlined in ADC before ADT and was transferred to all other images in the study with the DIR technique (Figure 27).

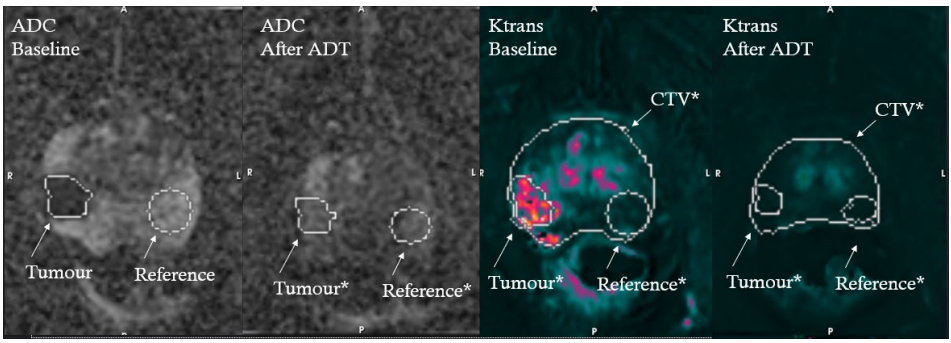

Figure 27. Tumour and reference VOI is outlined at baseline ADC. The CTV is outlined on T2w at baseline and then transferred to Ktrans. * indicates that the VOI is transferred with DIR from baseline. All images are from the PARAPLY study.

For first-order texture features, only ADC-defined features were significantly different between tumour and normal reference tissue after ADT. However, these differences are visually challenging (Figure 26). None of the GLCM texture features could differentiate between baseline-defined tumour VOI and normal reference tissue measured after ADT.

Hyaluronic acid-spacer, stability and rectum dosimetry

To evaluate the impact of an HA perirectal spacer on rectal dose as well as spacer stability during RT, we used repetitive MRI to track changes in HA shape and location (paper III).

The mean injected HA was 16±4 cm^3 (range 8–24) for the 52 patients in this part of the evaluation. The median time between HA injection and MR1 was one day (range 0–5). The HA thickness decreased significantly from MR1 to MR2/MR3, but no significant difference was seen between MR2 and MR3.

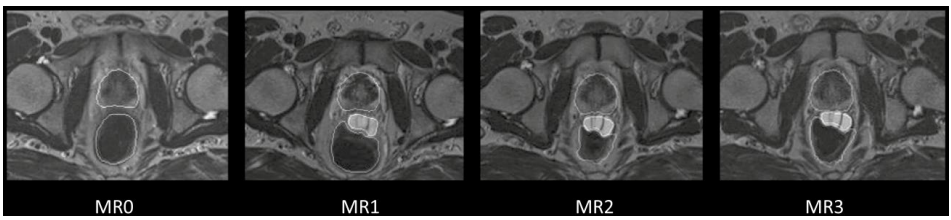

Figure 28. Example of T2w images in MR0/MR1/MR2/MR3 at the same level (base). HA is clearly visible between the rectum and CTV with a CRS 7/22/19/14 mm in MR0/MR1/MR2/MR3. HA thickness was 21/16/13 mm in MR1/MR2/MR3. MR1 was performed 1 day after HA, MR2 30 days and MR3 63 days after HA. CTV, rectum and HA are outlined. All images are from NOHARM study.

HA caused a significant increase in CTV-rectum Space from MR0 to MR1, MR2, and MR3. See images in Figure 28 for visualisation of the HA location between CTV and the rectum. However, CRS were significantly smaller in MR2 and MR3 compared to MR1, but no significant difference in CRS was seen between MR2 and MR3.

Dosimetry

Rectal V50%–V90% were significantly reduced with HA, although the reduction was not as pronounced in MR2 and MR3. No difference was seen for V50%–V90% between MR2 and MR3. See Figure 29 for mean dose volume histograms.

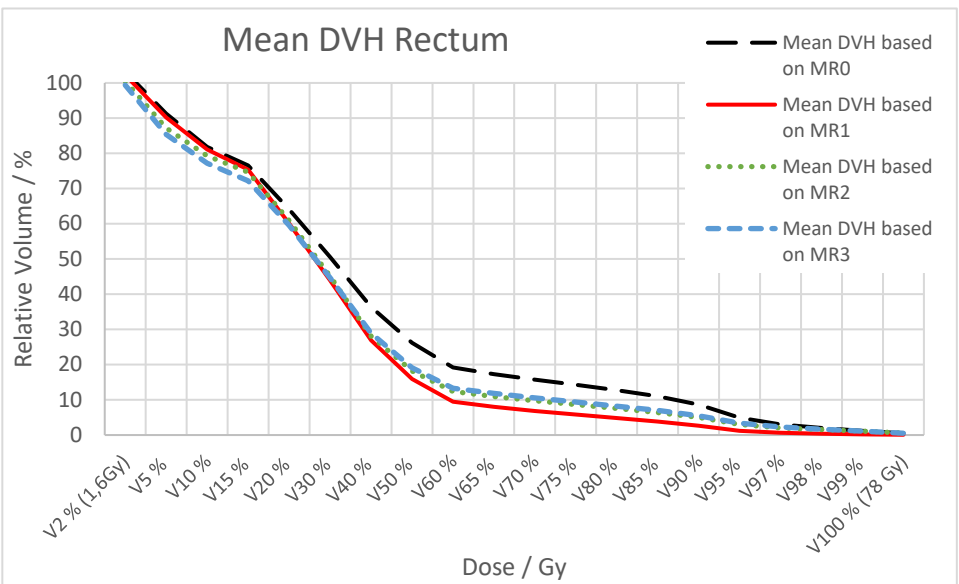

Figure 29. Mean Dose Volume Histograms (DVH). The black DVH is without HA. The red DVH is from TP with HA (MR1). The green DVH is based on MR2, and the blue DVH is based on MR3.

Pre-treatment imaging

To evaluate whether pre-treatment MRI and acetate-PET features can be associated with radiotherapy outcomes in high-risk/very high-risk PCa, we evaluated the quantifiable ADC end TLA_{max} values in the DIL. Seventy-six patients were included with a median follow-up time of 4.5 years [range: 1.3-7.7 years]. In total, there were 21 patients in the progression group and 55 in the non-progression group. For representative patient images, see Figure 30.

Figure 30. Pre-treatment imaging. Left: ADC with DIL^{ADC} marked with the blue arrow. Middel: T2w for anatomy visualisation only. Right: acetate PET/CT with two locations of DIL^{ACE} indicated by blue and green arrows. All images are from the PARAPLY study.

ADC did not differentiate between progression and no-progression groups in the pre-treatment images. The DIL-ADC values in progression and no-progression groups were 0.75 x 10^{-3} mm^2/s, and 0.74 x 10^{-3} mm^2/s, (95% CI: 0.71–0.78), respectively.

TLA_{max} for the progression group were 112 g (95% CI: 68.1–166.8), and for the progression-free group, 84.7 g (95% CI: 50.3–114.3). The SUV_{max} in the two groups were similar, and the functional tumour volume contributed to the TLA_{max} differences, but no significant differences could be measured.

In Figure 31, ADC and TLA_{max} in relation to PSA and progression are visualized. Neither ADC or TLA_{max} could be correlated to the outcome or initial PSA value.

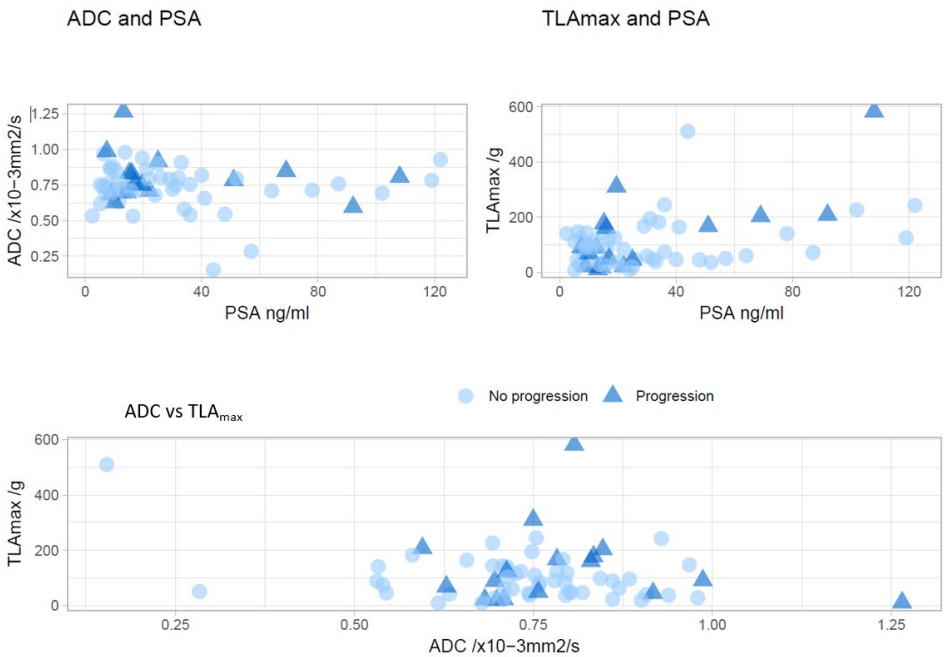

Figure 31. ADC and TLA_{max} in relation to progression and initial PSA. One patient with progression with an initial PSA of 281 ng/ml (ADC= 0.71, TLA_{max}=123) is not shown in the top row figures.

Discussion

This thesis aimed to solve problems that came to our notice from the MRI implementation in PCa RT and the clinical studies followed by MRI in RT planning. Four research questions were addressed: How to manage prostate and lymph nodes in the same target in WPRT? How can DIL-GTV be identified after ADT? How can the rectum dose be reasonable if the CTV/GTV is close to the prostate peripheries and the margins include parts of the rectum? Can pre-ADT imaging of the DIL-GTV correlate to progression for PCa? By adding all the pieces together, patients receiving PCa RT will hopefully benefit from these results.

Target imaging

For RT target imaging in PCa, the basic MRI sequences were used – T1w, T2w, and DWI with ADC– but not always with the same image quality requirements as a diagnostic mpMRI according to PI-RADS [7]. When imaging for TP, the disease is already localised and classified, and other quality measures, such as geometric accuracy [102], are more vital. DWI is very sensitive to the transitions between structures of different magnetic susceptibilities, such as air (gas in the rectum) and tissue. The large difference in susceptibility results in distorted images or a signal drop at the interfaces of these structures [39]. This is the reason for imaging DWI as early as possible in the sequence list after verifying that there is no gas in the rectum. T1w and T2w TSE sequences do not suffer from susceptibility transitions. In paper II, we used DIR to compensate for these distortions when the tumour VOI was outlined in ADC and then transferred with DIR to T2w and DCE.

Although ADC suffers from susceptibility issues, the sequence is included in every tumour imaging protocol due to its sensitivity to measure restricted diffusion [37]. PI-RADS [7] set an approximate ADC value of 0.75–0.90 $x10^{-3}mm^2/s$ as an aid for distinguishing benign from malignant prostatic lesions with a lower ADC for malignancies. To correlate ADC to patient outcome (paper IV), we measured the median ADC in DIL. ADC were 0.74 x 10^{-3} mm^2/s and 0.75 x 10^{-3} mm^2/s, respectively, depending on whether progression was evident. Furthermore, no statistical difference between the groups was shown, and no ADC correlation to the Gleason score or PSA was measured. In a review, Meyer et al. [103] found a weak to moderate inverse correlation between ADC values and Gleason score but urged for standardisation in imaging protocol. They suggest that a threshold for distinguishing malignant from benign lesions must be evaluated for every institution due to imaging protocol parameters and MRI equipment used. In a meta-analysis by Shaish et al. [104], ADC values show moderate accuracy in separating high-risk from low-risk PCa and also pointed out that the lack of

standardization in the imaging protocol results in difficulties comparing results from different studies.

The issue of reproducibility due to parameter choice in the MRI sequence and the hardware has clearly been shown [105, 106]. In 2019, A recommendation from Quantitative Imaging Biomarkers Alliance for DWI and DCE in oncology was published in JMRI [106], emphasizing the need for reproducibility and repeatability. In addition, a practical guide for radiomics in oncology was published in the journal RadioGraphics in 2021 [107]. In 2022, the Journal of Nuclear Medicine published a guideline from EANM/SNMMI [142] that provides researchers and clinicians with an updated and state-of-the-art relevant guide of good practices and recommendations for conducting radiomics studies in nuclear medicine imaging. Therefore, a standardization of imaging in clinical studies is hopefully coming.

Target movements

Although LNs appear normal in medical imaging, the micro spread might already exist and evolve into visible metastases on medical images. Moreira et al. [108] found that nearly 60% of patients diagnosed with nonmetastatic castration-resistant prostate cancer develop metastases over five years. The metastatic pathway in PCa is partly via the lymphatic system [28]. Therefore, Swedish national guidelines suggest WPRT to prevent metastasis, even for HR/VHR PCa patients without visible nodal involvement [2]. A recent outcome study (POP-RT) [74, 109] on elective WPRT for high-risk PCa compared WPRT to prostate-only RT for patients without LN engagement. The results show the five-year disease free survival was 89.5% with WPRT compared to 77.2% for prostate-only RT, and a higher metastasis-free survival for WPRT was also noted. POP-RT used a 7-mm margin to WPRT CTV in all directions and 5-7 mm for CTV in PORT with a bone anatomy registration procedure.

The prostate is not fixed to the bone, and fiducial markers are commonly used to compensate for inter-fraction motion [78-80]. In a large CTV comprising both the prostate and LN with margins, the use of fiducials to compensate for movements is a challenge. In paper I, we used MRI to track LN movements and found LN position shifts during RT. We showed that LN positions do not follow the prostate motion and are not fixed to bony structures.

A further development for paper I would be a treatment planning study elaborating on margins for WPRT by using the margin recipe by van Herk [63]. The margin recipe combines errors introduced by movements and daily patient set-up (random errors) and errors introduced in the treatment planning process (systematic errors). Marnouche et al. [110] evaluated margins for the pelvic LNs with the van Herk margin formula [63] and suggested the use of bony anatomy registration with a CTV-PTV margin for a prostate measuring 8 mm anterior-

posterior, 6 mm right-left, and 9 mm cranio-caudal. LN margins along the external and common iliac vessels were 4 mm and 5 mm, respectively. Marnouche et al. [110] did not recommend prostate-based registration due to the larger margins needed for the LN target volume. In paper I, we suggested variable margins due to movements both for the prostate fiducial registration and the bony anatomy registration technique. In bony registration, deviations for LNs were 1–4 mm right-left, 1–7 mm anterior-posterior, and 1–5 mm cranio-caudal, depending on location in the pelvis. Prostate movements were 2 mm right-left and 5 mm in the other directions in relation to bony anatomy. The drawback with bony registration is that prostate margins must be increased due to the motion. However, if a DIL-boost is included, the main focus should be the prostate target, whereas LN irradiation often is elective. In clinical practice at NUS, two registrations are performed daily – one on bones and one on fiducial markers. If the vector distance between the two registrations exceeds the CTV-PTV (8 mm) for the lymph node target at serial occasions, a re-planning is done with extended LN CTV-PTV margin because prostate CTV is the primary target. However, re-planning is very rare.

One solution to cope with inter- and intra-fractional prostate motion is real-time tracking with ultrasound [111], but it is not widely implemented in clinical practice. However, this technique does not solve the problem of independently moving targets inside a large CTV, although the prostate location will be clearly identified. Another solution for reducing movement margins is daily re-planning. With daily online adaptive RT [112], prostate inter-fractional movement is a minor problem, but this approach's issue with intra-fraction movements remains. The drawback of adaptive RT is increased clinical resources (outlining) and more time-consuming therapy sessions. The most accurate soft tissue imaging device is MRI. An MR-linac that uses MRI for target verification at treatment [113] would give the possibility to image LN directly. Moreover, the target could be re-planned with an adaptive approach [114], or MRI could be used for real-time tracking [115]. MR-linacs could be a game changer in RT workflow if the equipment becomes more time efficient and available to a larger patient population.

Target delineation

Even when inter- and intra- fractional movements are considered and included in PTV, the uncertainty for DIL-GTV outlining for additional boosting remains. ADT changes the tumour properties [43, 44, 69], influencing the image contrast (paper II) and making it hard to visually outline DIL-GTV after ADT. In clinical practice at NUS, ADT is given neoadjuvant and concomitant RT. This implies that MRI images without ADT are at least three months old when TP is performed,

and co-registration is difficult due to contrast and prostate size differences. This gives uncertainties in DIL-GTV location and extent.

A recent DIL-boost study (FLAME) [77] has shown improved biochemical progression-free survival for intermediate and high-risk PCa compared to non-boost RT. Only a minor part (8%) of the FLAME patients received neoadjuvant ADT, and the lack of contrast in MRI for DIL-GTV outlining after ADT was not an issue in FLAME [116].

DIL-GTV outlining after ADT is a problem. In paper II, we evaluated textural features for MR images after ADT for improved DIL outlining. Results in paper II show that first-order features are superior to GLCM features for DIL identification after ADT in ADC and contradict the results from a similar ADT MRI study by Daniel et al. [117]. One explanation of the differences between the results might be that Daniel et al. [13] evaluated two patient groups, one with and one without ADT. In paper II, we assessed the same patients before and after ADT. However, visual DIL-GTV identification after ADT is still a challenge.

One practical solution is the following hypothetical workflow: DIL-GTV should be identified and contoured in pre-ADT MRI. The diagnostic MRI performed when diagnosing PCa according to PI-RADS [7] can be used to guide DIL-GTV identification in pre-ADT MRI. Also, in pre-ADT MRI, fiducial markers are suggested to be implanted in the prostate for registration purposes in TP. The fiducial markers can be seen as three “landmarks” in the contrast-effected MRI. Then, the DIL-GTV contours should be propagated to post-ADT MRI images used for TP. Propagation techniques can be done manually or preferably with DIR, as in paper II with appropriate margins due to registration technique. It has also been shown in a review by von Eyben [76] that DIL volumes for boosting based on mpMRI have been underestimated compared to histopathological findings.

Another way to address this problem is to minimise the time between start of ADT and the planning MRI. If, for example, an androgen receptor antagonist could be used rather than the usual antagonist to reach castration status in the tissue in just a few days, the change in imaging features might be less pronounced. This approach, however, needs to be investigated both for feasibility and effect on the treatment.

If the DIL-GTV delineation is uncertain, a larger margin is needed. If PTV includes part of the rectum, this margin needs to be adjusted to minimize rectum side effects. When the distance between the prostate and rectum is increased, the dose coverage is easier to obtain and PTV needs fewer restrictions due to the rectum proximity. A recent study by Osman et al. [118] compared VMAT plans before and after spacer insertion in stereotactic ablative radiotherapy. The plan included a DIL boost in 5 fractions with 40 Gy to the prostate CTV combined with a simultaniouis integrated boost to DIL up to 50 Gy. For 25% of the patients, a

higher DIL boost was achieved with a spacer. Furthermore, a significant reduction in rectal dose and better target coverage was reached for all patients. The dose reduction to the rectum is in line with our results in paper III. We showed that hyaluronic acid as a spacer between the prostate and rectum proved safe and reduced the rectum dose. The use of spacers in the clinic has not been universally accepted [119, 120] and is still under review in Sweden [2]. However, a spacer may be beneficial especially when higher doses are delivered in fewer fractions, such as in hypofractionated treatment [118, 121].

Strengths and weaknesses of this doctoral project

All studies were planned more than ten years ago, which is both a strength and a weakness. The technical development in MRI and RT has improved significantly over the years. However, this time span is needed to evaluate treatment outcomes in a generally slow-developing disease such as prostate cancer. Therefore, these types of studies are needed even though the techniques continue to develop. Two of the studies have a minimum of five-year follow-up after RT, which is a strength, although for high-risk patients, as in paper IV, this might not be enough in regard to oncological outcome. The PI-RADS, which is widely used today, was not implemented when we started papers II and IV, so the MRI parameters are not precisely comparable to today's recommendations. However, the image quality is acceptable and can be interpreted according to today's standards. Nonetheless, comparing ADC today is complicated between studies and between different MRI vendors even with the PI-RADS recommendations. The field is ever developing and the PI-RADS have also changed over the years and have been using version 2.1 since 2019.

Another limitation is the relatively small sample sizes in papers I, II, and IV, and the statistical outcome must be interpreted with care. Study IV will be continued with a collection of a reference group without boosting or lymph node irradiation, and outcome comparisons will be conducted.

Future perspectives

Radiotherapy has become more individualized with, for example, MRI, allowing the boosting of specific targets inside CTV that are not visible with CT. The MRI technique has made enormous progress in recent years with deep learning algorithms for image improvements and faster imaging. A further development would be to implement this MRI technique into DIL identification. With improved imaging techniques and perhaps quantifiable T2w, texture analysis might improve DIL identification after ADT. Therefore, an updated study including MRI, histopathology, and outcome for PCa with deep learning algorithms for MRI would be interesting.

However, the clinical value is limited if we do not work with robust and reproducible data concerning interpretation, technical differences, image parameters, and reconstruction alternatives. This challenge needs to be addressed. Furthermore, with personalised treatments, the evaluations will be more complex, and collaboration platforms to handle all information (imaging, biology, patient-reported outcome) will be more efficient. Moreover, collaboration between different specialities becomes easier with a common platform.

Conclusions

This thesis includes four papers involving MRI and its use and usefulness in PCa radiotherapy. Using MRIs, we measured lymph node and prostate movements during RT and found that margins due to motion alter in the pelvic region. Image contrast after hormone therapy was evaluated. Surprisingly, no additional benefit from texture analysis in differentiation between normal tissue and intra-prostatic tumour lesion was observed. Using MRI, we measured hyaluronic spacer stability during RT, and a dose reduction to the rectum was accomplished with the spacer even though the spacer was not stable during RT. Baseline MRI diffusion (i.e., before ADT and RT) was evaluated with respect to patient outcomes in a high-risk/very high-risk PCa group, but the ADC in relation to outcome could not be established.

To conclude, clinically relevant adjustments can be implemented with the gathered knowledge about the target in PCa. HA spacer is safe and efficient, margins can be variable in WPRT, and DIL should be identified before ADT.

Acknowledgements

En avhandling är ett individuellt lagarbete! Tack till alla som arbetat med och deltagit i MOVE, PARAPLY och NOHARM studierna. Ert bidrag är ovärderligt!

Ett stort tack till mina handledare i Umeå, Camilla Thellenberg-Karlsson, Tufve Nyholm, Joakim Jonson samt min handledare i Sundsvall Lars Beckman för ert engagemang och stöd under doktorandtiden! Imponerad över er kapacitet och hoppas på framtida samarbeten! Ett stort tack även till mina medförfattare på de artiklar som producerats, jag har lärt mig mycket från er!

Jag vill även tacka mina nuvarande och dåvarande chefer och kollegor på Sjukhusfysik för att jag fått den här möjligheten, för att ni alltid ställt upp och täckt upp för mig under doktorandtiden! Det gäller även alla arbetskamrater på MR-enheterna i RVN, ni gör arbetet så roligt och omväxlande! Sedan vill jag tacka mina doktorandkompisar, speciellt Ulrika och Kristina för roliga stunder, textgranskning och pepp!

För all "runt omkring hjälp" vill jag tacka Maria Wing, du har guidat mig genom administrationen och fixat så att allt funkar även då man sitter på distans hela tiden!

Jag vill rikta en speciell hälsning till Henrik Bergman, utan ditt engagemang och hjälp med den första studien skulle jag aldrig ha gett mig in i det här projektet.

Tack även till Stiftelsen Emil Anderssons fond för medicinsk forskning, Henry Kjelléns minnesfond, Cancerforskningsfonden i Norrland samt FoU i RVN för det generösa stöd som möjliggjort detta arbete.

Sist men inte minst vill jag tacka mina nära och kära! Nu när sista raden är skriven i denna avhandling ska jag ta lite ledigt eller som citatmaskinen Albert (5 år) sa, ska leta upp ett jobb att undvika…

References

[1] Cancerfonden. https://www.cancerfonden.se/om-cancer/cancersjukdomar/prostatacancer.
[2] Regionala-cancercentrum. NVP-Prostatacancer. 2022.
[3] Chopra S, Toi A, Taback N, Evans A, Haider MA, Milosevic M, et al. Pathological predictors for site of local recurrence after radiotherapy for prostate cancer. Int J Radiat Oncol Biol Phys. 2012;82:e441-8.
[4] Pucar D, Hricak H, Shukla-Dave A, Kuroiwa K, Drobnjak M, Eastham J, et al. Clinically significant prostate cancer local recurrence after radiation therapy occurs at the site of primary tumor: magnetic resonance imaging and step-section pathology evidence. Int J Radiat Oncol Biol Phys. 2007;69:62-9.
[5] Helsinki WMADo. World Medical Association Declaration of Helsinki: ethical principles for medical research involving human subjects. JAMA Netw Open. 2013;310:2191-4.
[6] McRobbie DW. MRI From Picture to Proton. 2 ed: Cambridge University Press; 2009.
[7] Radiology ACo. PI-RADS v.2.1. 2019.
[8] Hall EJ, Giaccia AJ. Radiobiology for the radiologist, 4th ed. Philadelphia: Lippincott Williams & Wilkings, Wolters Kluwert1994.
[9] Hejmadi M. Introduction-to-cancer-biology. 2 ed2010.
[10] Hanahan D, Weinberg RA. Hallmarks of cancer: the next generation. Cell. 2011;144:646-74.
[11] Basu AK. DNA Damage, Mutagenesis and Cancer. Int J Mol Sci. 2018;19.
[12] Solimando AG, Kalogirou C, Krebs M. Angiogenesis as Therapeutic Target in Metastatic Prostate Cancer - Narrowing the Gap Between Bench and Bedside. Front Immunol. 2022;13:842038.
[13] Folkman J. Tumor angiogenesis: therapeutic implications. N Engl J Med. 1971;285:1182-6.
[14] Bergers G, Fendt SM. The metabolism of cancer cells during metastasis. Nat Rev Cancer. 2021;21:162-80.
[15] Lomax ME, Folkes LK, O'Neill P. Biological consequences of radiation-induced DNA damage: relevance to radiotherapy. Clin Oncol (R Coll Radiol). 2013;25:578-85.
[16] Stone HB, Coleman CN, Anscher MS, McBride WH. Effects of radiation on normal tissue: consequences and mechanisms. Lancet Oncol. 2003;4:529-36.
[17] Krol R, Smeenk RJ, van Lin EN, Hopman WP. Impact of late anorectal dysfunction on quality of life after pelvic radiotherapy. Int J Colorectal Dis. 2013;28:519-26.
[18] Lee CH, Akin-Olugbade O, Kirschenbaum A. Overview of prostate anatomy, histology, and pathology. Endocrinol Metab Clin North Am. 2011;40:565-75, viii-ix.
[19] Selman SH. The McNeal prostate: a review. Urology. 2011;78:1224-8.
[20] Wilson AH. The prostate gland: a review of its anatomy, pathology, and treatment. JAMA. 2014;312:562.
[21] Ittmann M. Anatomy and Histology of the Human and Murine Prostate. Cold Spring Harb Perspect Med. 2018;8.
[22] Brawer MK. Androgen deprivation therapy: a cornerstone in the treatment of advanced prostate cancer. Rev Urol. 2004;6 Suppl 8:S3-9.

[23] 1177. Blodprov: PSA. 2023.
[24] Balk SP, Ko YJ, Bubley GJ. Biology of prostate-specific antigen. J Clin Oncol. 2003;21:383-91.
[25] Wolff JM, Bares R, Jung PK, Buell U, Jakse G. Prostate-specific antigen as a marker of bone metastasis in patients with prostate cancer. Urol Int. 1996;56:169-73.
[26] Control UfIC. TNM cancer staging system.
[27] Taylor A, Rockall AG, Powell ME. An atlas of the pelvic lymph node regions to aid radiotherapy target volume definition. Clin Oncol (R Coll Radiol). 2007;19:542-50.
[28] Bubendorf L, Schopfer A, Wagner U, Sauter G, Moch H, Willi N, et al. Metastatic patterns of prostate cancer: an autopsy study of 1,589 patients. Hum Pathol. 2000;31:578-83.
[29] Epstein JI, Egevad L, Amin MB, Delahunt B, Srigley JR, Humphrey PA, et al. The 2014 International Society of Urological Pathology (ISUP) Consensus Conference on Gleason Grading of Prostatic Carcinoma: Definition of Grading Patterns and Proposal for a New Grading System. Am J Surg Pathol. 2016;40:244-52.
[30] Westbrook C. Handbook of MRI Technique. 4 ed: John Wiley & Sons; 2014.
[31] Michael L. Handbook of Nuclear Medicine and Molecular Imaging for Physicists : Instrumentation and Imaging Procedures, Volume I. Boca Raton: CRC Press; 2021.
[32] Ray Hashman Hashemi, J. LC, William G. Bradley. MRI the basics: Lww; 2003.
[33] Elster A. Questions and Answers in MRI. 2023.
[34] Baur ADJ, Hansen CM, Rogasch J, Posch H, Elezkurtaj S, Maxeiner A, et al. Evaluation of T1 relaxation time in prostate cancer and benign prostate tissue using a Modified Look-Locker inversion recovery sequence. Sci Rep. 2020;10:3121.
[35] Chatterjee A, Devaraj A, Mathew M, Szasz T, Antic T, Karczmar GS, et al. Performance of T2 Maps in the Detection of Prostate Cancer. Acad Radiol. 2019;26:15-21.
[36] Borren A, Moman MR, Groenendaal G, Boeken Kruger AE, van Diest PJ, van der Groep P, et al. Why prostate tumour delineation based on apparent diffusion coefficient is challenging: an exploration of the tissue microanatomy. Acta Oncol. 2013;52:1629-36.
[37] Koh DM, Collins DJ. Diffusion-weighted MRI in the body: applications and challenges in oncology. AJR Am J Roentgenol. 2007;188:1622-35.
[38] Sorace AG, Elkassem AA, Galgano SJ, Lapi SE, Larimer BM, Partridge SC, et al. Imaging for Response Assessment in Cancer Clinical Trials. Semin Nucl Med. 2020;50:488-504.
[39] Plodeck V, Radosa CG, Hubner HM, Baldus C, Borkowetz A, Thomas C, et al. Rectal gas-induced susceptibility artefacts on prostate diffusion-weighted MRI with epi read-out at 3.0 T: does a preparatory micro-enema improve image quality? Abdom Radiol (NY). 2020;45:4244-51.
[40] Rosenkrantz AB, Taneja SS. Radiologist, be aware: ten pitfalls that confound the interpretation of multiparametric prostate MRI. AJR Am J Roentgenol. 2014;202:109-20.
[41] Alonzi R, Padhani AR, Allen C. Dynamic contrast enhanced MRI in prostate cancer. Eur J Radiol. 2007;63:335-50.
[42] Reuter VE. Pathological changes in benign and malignant prostatic tissue following androgen deprivation therapy. Urology. 1997;49:16-22.

[43] Hotker AM, Mazaheri Y, Zheng J, Moskowitz CS, Berkowitz J, Lantos JE, et al. Prostate Cancer: assessing the effects of androgen-deprivation therapy using quantitative diffusion-weighted and dynamic contrast-enhanced MRI. Eur Radiol. 2015;25:2665-72.
[44] Kim AY, Kim CK, Park SY, Park BK. Diffusion-weighted imaging to evaluate for changes from androgen deprivation therapy in prostate cancer. AJR Am J Roentgenol. 2014;203:W645-50.
[45] Michael L. Handbook of Nuclear Medicine and Molecular Imaging for Physicists : Radiopharmaceuticals and Clinical Applications, Volume III. [Place of publication not identified]: CRC Press; 2021.
[46] Wadsak W, Mitterhauser M. Basics and principles of radiopharmaceuticals for PET/CT. Eur J Radiol. 2010;73:461-9.
[47] Basu S, Hess S, Nielsen Braad PE, Olsen BB, Inglev S, Hoilund-Carlsen PF. The Basic Principles of FDG-PET/CT Imaging. PET Clin. 2014;9:355-70, v.
[48] Mohsen B, Giorgio T, Rasoul ZS, Werner L, Ali GR, Reza DK, et al. Application of C-11-acetate positron-emission tomography (PET) imaging in prostate cancer: systematic review and meta-analysis of the literature. BJU Int. 2013;112:1062-72.
[49] Spick C, Herrmann K, Czernin J. Evaluation of Prostate Cancer with 11C-Acetate PET/CT. J Nucl Med. 2016;57:30S-7S.
[50] Kato T, Tsukamoto E, Kuge Y, Takei T, Shiga T, Shinohara N, et al. Accumulation of [11C]acetate in normal prostate and benign prostatic hyperplasia: comparison with prostate cancer. Eur J Nucl Med Mol Imaging. 2002;29:1492-5.
[51] Kinahan PE, Fletcher JW. Positron emission tomography-computed tomography standardized uptake values in clinical practice and assessing response to therapy. Semin Ultrasound CT MR. 2010;31:496-505.
[52] Michael L. Handbook of Nuclear Medicine and Molecular Imaging for Physicists : Modelling, Dosimetry and Radiation Protection, Volume II. [Place of publication not identified]: CRC Press; 2021.
[53] Tsechelidis I, Vrachimis A. PSMA PET in Imaging Prostate Cancer. Front Oncol. 2022;12:831429.
[54] Haberkorn U, Eder M, Kopka K, Babich JW, Eisenhut M. New Strategies in Prostate Cancer: Prostate-Specific Membrane Antigen (PSMA) Ligands for Diagnosis and Therapy. Clin Cancer Res. 2016;22:9-15.
[55] Emonds KM, Swinnen JV, Lerut E, Koole M, Mortelmans L, Mottaghy FM. Evaluation of androgen-induced effects on the uptake of [18F]FDG, [11C]choline and [11C]acetate in an androgen-sensitive and androgen-independent prostate cancer xenograft model. EJNMMI Res. 2013;3:31.
[56] Sudhyadhom A. On the molecular relationship between Hounsfield Unit (HU), mass density, and electron density in computed tomography (CT). PLoS One. 2020;15:e0244861.
[57] Kerkmeijer LGW, Maspero M, Meijer GJ, van der Voort van Zyp JRN, de Boer HCJ, van den Berg CAT. Magnetic Resonance Imaging only Workflow for Radiotherapy Simulation and Planning in Prostate Cancer. Clin Oncol (R Coll Radiol). 2018;30:692-701.
[58] Johnstone E, Wyatt JJ, Henry AM, Short SC, Sebag-Montefiore D, Murray L, et al. Systematic Review of Synthetic Computed Tomography Generation Methodologies for

Use in Magnetic Resonance Imaging-Only Radiation Therapy. Int J Radiat Oncol Biol Phys. 2018;100:199-217.
[59] Jonsson J, Nyholm T, Soderkvist K. The rationale for MR-only treatment planning for external radiotherapy. Clin Transl Radiat Oncol. 2019;18:60-5.
[60] 50 I. ICRU-50-Prescribing-Recording-and-Reporting-Photon-Beam-Therapy.
[61] 62 I. Icru-Report-62.
[62] Dubois DF, Prestidge BR, Hotchkiss LA, Prete JJ, Bice WS, Jr. Intraobserver and interobserver variability of MR imaging- and CT-derived prostate volumes after transperineal interstitial permanent prostate brachytherapy. Radiology. 1998;207:785-9.
[63] van Herk M. Errors and margins in radiotherapy. Semin Radiat Oncol. 2004;14:52-64.
[64] Menard C, Paulson E, Nyholm T, McLaughlin P, Liney G, Dirix P, et al. Role of Prostate MR Imaging in Radiation Oncology. Radiol Clin North Am. 2018;56:319-25.
[65] Wegener D, Zips D, Thorwarth D, Weiss J, Othman AE, Grosse U, et al. Precision of T2 TSE MRI-CT-image fusions based on gold fiducials and repetitive T2 TSE MRI-MRI-fusions for adaptive IGRT of prostate cancer by using phantom and patient data. Acta Oncol. 2019;58:88-94.
[66] Crehange G, Mirjolet C, Gauthier M, Martin E, Truc G, Peignaux-Casasnovas K, et al. Clinical impact of margin reduction on late toxicity and short-term biochemical control for patients treated with daily on-line image guided IMRT for prostate cancer. Radiother Oncol. 2012;103:244-6.
[67] Sandhu S, Moore CM, Chiong E, Beltran H, Bristow RG, Williams SG. Prostate cancer. Lancet. 2021;398:1075-90.
[68] Palacios DA, Miyake M, Rosser CJ. Radiosensitization in prostate cancer: mechanisms and targets. BMC Urol. 2013;13:4.
[69] Barrett T, Gill AB, Kataoka MY, Priest AN, Joubert I, McLean MA, et al. DCE and DW MRI in monitoring response to androgen deprivation therapy in patients with prostate cancer: a feasibility study. Magn Reson Med. 2012;67:778-85.
[70] Aly M, Leval A, Schain F, Liwing J, Lawson J, Vago E, et al. Survival in patients diagnosed with castration-resistant prostate cancer: a population-based observational study in Sweden. Scand J Urol. 2020;54:115-21.
[71] Isbarn H, Boccon-Gibod L, Carroll PR, Montorsi F, Schulman C, Smith MR, et al. Androgen deprivation therapy for the treatment of prostate cancer: consider both benefits and risks. Eur Urol. 2009;55:62-75.
[72] Zapatero A, Guerrero A, Maldonado X, Alvarez A, Gonzalez San Segundo C, Cabeza Rodriguez MA, et al. High-dose radiotherapy with short-term or long-term androgen deprivation in localised prostate cancer (DART01/05 GICOR): a randomised, controlled, phase 3 trial. Lancet Oncol. 2015;16:320-7.
[73] Widmark A, Gunnlaugsson A, Beckman L, Thellenberg-Karlsson C, Hoyer M, Lagerlund M, et al. Ultra-hypofractionated versus conventionally fractionated radiotherapy for prostate cancer: 5-year outcomes of the HYPO-RT-PC randomised, non-inferiority, phase 3 trial. The Lancet. 2019;394:385-95.
[74] Murthy V, Maitre P, Kannan S, Panigrahi G, Krishnatry R, Bakshi G, et al. Prostate-Only Versus Whole-Pelvic Radiation Therapy in High-Risk and Very High-Risk Prostate

Cancer (POP-RT): Outcomes From Phase III Randomized Controlled Trial. J Clin Oncol. 2021;39:1234-42.
[75] Wang S, Tang W, Luo H, Jin F, Wang Y. Efficacy and Toxicity of Whole Pelvic Radiotherapy Versus Prostate-Only Radiotherapy in Localized Prostate Cancer: A Systematic Review and Meta-Analysis. Front Oncol. 2021;11:796907.
[76] von Eyben FE, Kiljunen T, Kangasmaki A, Kairemo K, von Eyben R, Joensuu T. Radiotherapy Boost for the Dominant Intraprostatic Cancer Lesion-A Systematic Review and Meta-Analysis. Clin Genitourin Cancer. 2016;14:189-97.
[77] Kerkmeijer LGW, Groen VH, Pos FJ, Haustermans K, Monninkhof EM, Smeenk RJ, et al. Focal Boost to the Intraprostatic Tumor in External Beam Radiotherapy for Patients With Localized Prostate Cancer: Results From the FLAME Randomized Phase III Trial. J Clin Oncol. 2021;39:787-96.
[78] Byrne TE. A review of prostate motion with considerations for the treatment of prostate cancer. Med Dosim. 2005;30:155-61.
[79] McPartlin AJ, Li XA, Kershaw LE, Heide U, Kerkmeijer L, Lawton C, et al. MRI-guided prostate adaptive radiotherapy - A systematic review. Radiother Oncol. 2016;119:371-80.
[80] Langen KM, Jones DT. Organ motion and its management. Int J Radiat Oncol Biol Phys. 2001;50:265-78.
[81] Harris VA, Staffurth J, Naismith O, Esmail A, Gulliford S, Khoo V, et al. Consensus Guidelines and Contouring Atlas for Pelvic Node Delineation in Prostate and Pelvic Node Intensity Modulated Radiation Therapy. Int J Radiat Oncol Biol Phys. 2015;92:874-83.
[82] Taylor A, Rockall AG, Reznek RH, Powell ME. Mapping pelvic lymph nodes: guidelines for delineation in intensity-modulated radiotherapy. Int J Radiat Oncol Biol Phys. 2005;63:1604-12.
[83] Pano B, Sebastia C, Bunesch L, Mestres J, Salvador R, Macias NG, et al. Pathways of lymphatic spread in male urogenital pelvic malignancies. Radiographics. 2011;31:135-60.
[84] Hou Z, Li G, Bai S. High dose versus conventional dose in external beam radiotherapy of prostate cancer: a meta-analysis of long-term follow-up. J Cancer Res Clin Oncol. 2015;141:1063-71.
[85] Prada PJ, Fernandez J, Martinez AA, de la Rua A, Gonzalez JM, Fernandez JM, et al. Transperineal injection of hyaluronic acid in anterior perirectal fat to decrease rectal toxicity from radiation delivered with intensity modulated brachytherapy or EBRT for prostate cancer patients. Int J Radiat Oncol Biol Phys. 2007;69:95-102.
[86] Tang Q, Zhao F, Yu X, Wu L, Lu Z, Yan S. The role of radioprotective spacers in clinical practice: a review. Quant Imaging Med Surg. 2018;8:514-24.
[87] Miller LE, Efstathiou JA, Bhattacharyya SK, Payne HA, Woodward E, Pinkawa M. Association of the Placement of a Perirectal Hydrogel Spacer With the Clinical Outcomes of Men Receiving Radiotherapy for Prostate Cancer: A Systematic Review and Meta-analysis. JAMA Netw Open. 2020;3:e208221.
[88] Whalley D, Hruby G, Alfieri F, Kneebone A, Eade T. SpaceOAR Hydrogel in Dose-escalated Prostate Cancer Radiotherapy: Rectal Dosimetry and Late Toxicity. Clin Oncol (R Coll Radiol). 2016;28:e148-54.

[89] Hwang ME, Black PJ, Elliston CD, Wolthuis BA, Smith DR, Wu CC, et al. A novel model to correlate hydrogel spacer placement, perirectal space creation, and rectum dosimetry in prostate stereotactic body radiotherapy. Radiat Oncol. 2018;13:192.
[90] Te Velde BL, Westhuyzen J, Awad N, Wood M, Shakespeare TP. Late toxicities of prostate cancer radiotherapy with and without hydrogel SpaceAOR insertion. J Med Imaging Radiat Oncol. 2019;63:836-41.
[91] Klein S, Staring M, Murphy K, Viergever MA, Pluim JP. elastix: a toolbox for intensity-based medical image registration. IEEE Trans Med Imaging. 2010;29:196-205.
[92] Oh S, Kim S. Deformable image registration in radiation therapy. Radiat Oncol J. 2017;35:101-11.
[93] Zitová B, Flusser J. Image registration methods: a survey. Image Vision Comput. 2003;21:977-1000.
[94] Lofstedt T, Brynolfsson P, Asklund T, Nyholm T, Garpebring A. Gray-level invariant Haralick texture features. PLoS One. 2019;14:e0212110.
[95] Yang F, Ford JC, Dogan N, Padgett KR, Breto AL, Abramowitz MC, et al. Magnetic resonance imaging (MRI)-based radiomics for prostate cancer radiotherapy. Transl Androl Urol. 2018;7:445-58.
[96] Stoyanova R, Takhar M, Tschudi Y, Ford JC, Solorzano G, Erho N, et al. Prostate cancer radiomics and the promise of radiogenomics. Transl Cancer Res. 2016;5:432-47.
[97] Peeken JC, Bernhofer M, Wiestler B, Goldberg T, Cremers D, Rost B, et al. Radiomics in radiooncology - Challenging the medical physicist. Phys Med. 2018;48:27-36.
[98] Lambin P, Rios-Velazquez E, Leijenaar R, Carvalho S, van Stiphout RG, Granton P, et al. Radiomics: extracting more information from medical images using advanced feature analysis. Eur J Cancer. 2012;48:441-6.
[99] Patel N, Henry A, Scarsbrook A. The value of MR textural analysis in prostate cancer. Clin Radiol. 2019;74:876-85.
[100] Brynolfsson P, Nilsson D, Torheim T, Asklund T, Karlsson CT, Trygg J, et al. Haralick texture features from apparent diffusion coefficient (ADC) MRI images depend on imaging and pre-processing parameters. Sci Rep. 2017;7:4041.
[101] Garpebring A, Brynolfsson P, Kuess P, Georg D, Helbich TH, Nyholm T, et al. Density estimation of grey-level co-occurrence matrices for image texture analysis. Phys Med Biol. 2018;63:195017.
[102] Kavaluus H, Nousiainen K, Kaijaluoto S, Seppala T, Saarilahti K, Tenhunen M. Determination of acceptance criteria for geometric accuracy of magnetic resonance imaging scanners used in radiotherapy planning. Phys Imaging Radiat Oncol. 2021;17:58-64.
[103] Meyer HJ, Wienke A, Surov A. Discrimination between clinical significant and insignificant prostate cancer with apparent diffusion coefficient - a systematic review and meta analysis. BMC Cancer. 2020;20:482.
[104] Shaish H, Kang SK, Rosenkrantz AB. The utility of quantitative ADC values for differentiating high-risk from low-risk prostate cancer: a systematic review and meta-analysis. Abdom Radiol (NY). 2017;42:260-70.
[105] Hoang-Dinh A, Nguyen-Quang T, Bui-Van L, Gonindard-Melodelima C, Souchon R, Rouviere O. Reproducibility of apparent diffusion coefficient measurement in normal prostate peripheral zone at 1.5T MRI. Diagn Interv Imaging. 2022;103:545-54.

[106] Shukla-Dave A, Obuchowski NA, Chenevert TL, Jambawalikar S, Schwartz LH, Malyarenko D, et al. Quantitative imaging biomarkers alliance (QIBA) recommendations for improved precision of DWI and DCE-MRI derived biomarkers in multicenter oncology trials. J Magn Reson Imaging. 2019;49:e101-e21.
[107] Shur JD, Doran SJ, Kumar S, Ap Dafydd D, Downey K, O'Connor JPB, et al. Radiomics in Oncology: A Practical Guide. Radiographics. 2021;41:1717-32.
[108] Moreira DM, Howard LE, Sourbeer KN, Amarasekara HS, Chow LC, Cockrell DC, et al. Predictors of Time to Metastasis in Castration-resistant Prostate Cancer. Urology. 2016;96:171-6.
[109] Murthy V, Maitre P, Bhatia J, Kannan S, Krishnatry R, Prakash G, et al. Late toxicity and quality of life with prostate only or whole pelvic radiation therapy in high risk prostate cancer (POP-RT): A randomised trial. Radiother Oncol. 2020;145:71-80.
[110] Marnouche EA, Hadadi K, Abdelhak M, Benlemlih M, Hommadi M, Zaghba N, et al. Evaluation of margins in pelvic lymph nodes and prostate radiotherapy and the impact of bladder and rectum on prostate position. Cancer Radiother. 2021;25:161-8.
[111] Sihono DSK, Ehmann M, Heitmann S, von Swietochowski S, Grimm M, Boda-Heggemann J, et al. Determination of Intrafraction Prostate Motion During External Beam Radiation Therapy With a Transperineal 4-Dimensional Ultrasound Real-Time Tracking System. Int J Radiat Oncol Biol Phys. 2018;101:136-43.
[112] Antico M, Prinsen P, Cellini F, Fracassi A, Isola AA, Cobben D, et al. Real-time adaptive planning method for radiotherapy treatment delivery for prostate cancer patients, based on a library of plans accounting for possible anatomy configuration changes. PLoS One. 2019;14:e0213002.
[113] Sritharan K, Tree A. MR-guided radiotherapy for prostate cancer: state of the art and future perspectives. Br J Radiol. 2022;95:20210800.
[114] Cunningham JM, Chin Snyder K, Kim JP, Siddiqui SM, Parikh P, Chetty IJ, et al. On-line adaptive and real-time intrafraction motion management of spine-SBRT on an MR-linac. FrPhy. 2022;10.
[115] Keiper TD, Tai A, Chen X, Paulson E, Lathuiliere F, Beriault S, et al. Feasibility of real-time motion tracking using cine MRI during MR-guided radiation therapy for abdominal targets. Med Phys. 2020;47:3554-66.
[116] van Schie MA, Dinh CV, Houdt PJV, Pos FJ, Heijmink S, Kerkmeijer LGW, et al. Contouring of prostate tumors on multiparametric MRI: Evaluation of clinical delineations in a multicenter radiotherapy trial. Radiother Oncol. 2018;128:321-6.
[117] Daniel M, Kuess P, Andrzejewski P, Nyholm T, Helbich T, Polanec S, et al. Impact of androgen deprivation therapy on apparent diffusion coefficient and T2w MRI for histogram and texture analysis with respect to focal radiotherapy of prostate cancer. Strahlenther Onkol. 2019;195:402-11.
[118] Osman SOS, Fairmichael C, Whitten G, Lundy GS, Wesselman R, Wilson ML, et al. Simultaneous integrated boost (SIB) to dominant intra-prostatic lesions during extreme hypofractionation for prostate cancer: the impact of rectal spacers. Radiat Oncol. 2022;17:38.
[119] Levy JF, Khairnar R, Louie AV, Showalter TN, Mullins CD, Mishra MV. Evaluating the Cost-Effectiveness of Hydrogel Rectal Spacer in Prostate Cancer Radiation Therapy. Pract Radiat Oncol. 2019;9:e172-e9.

[120] Vanneste BG, Pijls-Johannesma M, Van De Voorde L, van Lin EN, van de Beek K, van Loon J, et al. Spacers in radiotherapy treatment of prostate cancer: is reduction of toxicity cost-effective? Radiother Oncol. 2015;114:276-81.
[121] Pepe P, Tamburo M, Pennisi M, Marletta D, Marletta F. Clinical Outcomes of Hydrogel Spacer Injection Space OAR in Men Submitted to Hypofractionated Radiotherapy for Prostate Cancer. In Vivo. 2021;35:3385-9.